UNIVERSITY OF CALIFORNIA,
IRVINE

The Effect of Co, Ni, and Cr Impurities on the Electronic Properties of Iron Pyrite

THESIS

submitted in partial satisfaction of the requirements
for the degree of

MASTER OF SCIENCES

in Physics

by

Trenton Salk

Thesis Committee:
Professor Matt Law, Chair
Professor Shane Ardo
Professor Reginald Penner

2019

DEDICATION

To

Open Mike Eagle

Because someone promised you they would,
but didn't.

TABLE OF CONTENTS

LIST OF FIGURES

LIST OF TABLES

ACKNOWLEDGMENTS

I'd like to thank my committee chair and advisor, Matt Law, for his guidance, patience and support.

To my lab mates I've had over the years: Dr. Moritz Limpinsel, Dr. Vineet Nair, Dr. Jason Tolentino, Dr. Nima Farhi, Dr. Amanda Weber, Mohammed El Makkaoui, Dr. Zhongyue Laun, Dr. Kan Fu, Glen Junor, Alex Ableson, Dr. Christian Engelbrekt, Dr. Darren Neo, Dr. Chao Yi, Caroline Qian, Yash Gargasya, and Andy Yang, thank you all for your help and camaraderie.

A special thank you to my friends and family for their love, support, and encouragement.

ABSTRACT OF THE THESIS

Iron Pyrite Single Crystal Studies

By

Trenton Salk

Master of Science in Physics

University of California, Irvine, 2019

Professor Matt Law Irvine, Chair

Iron pyrite (FeS_2) is an earth-abundant, non-toxic material that has a suitable band gap of 0.95 eV, a large optical absorption coefficient, and adequate carrier diffusion lengths for use in photovoltaic applications. However, its practical use is limited in part by poor understanding and control of doping. Here, we employ variable temperature Hall effect and conductivity to study, in detail, the impact of three transition metal impurities (cobalt, nickel, and chromium) on the electric properties of ultrapure pyrite single crystals grown in sodium polysulfide. By studying samples as a function of impurity concentration, we conclusively establish that cobalt is a nearly ideal donor in the dilute limit (<500 ppm Co) with a defect state that lies ~70-110 meV above the conduction band minimum, while nickel and chromium act as deep donors that barely affect the carrier concentration. These results establish the basic doping behavior of three elements and provide a pathway for overcoming the key challenges to rational doping in pyrite.

Chapter 1

Introduction

1.1 The Energy Crisis and Solar Power

In 2018 global energy consumption was 18.6 terrawatts (TW), up 2.9% from 2017, the largest rise seen in the past decade [1]. While generation of energy expanded for almost all sources, nearly 70% of this increased demand was met by fossil fuels. As a result, global energy-related CO_2 emissions rose by 1.7%. Experts project global energy consumption to increase an additional 50% by 2050 [2]. One of the greatest challenges of our time is to meet this growing demand without further damaging the environment and polluting our environment by finding cheap, clean and safe alternatives to fossil and nuclear fuels. Solar energy has the ability to meet these conditions and provide the world with the power it needs.

Over 10^4 TW solar energy strikes the earth's surface each year. Less than 2 hours of radiation from the sun has enough potential energy to meet global demands for a year. While there are several methods used in attempts to harness this energy including solar thermal (using heat from the sun to heat a medium) and solar fuel production (using solar light to drive

photochemical reactions), the most well-known method is to utilize the photovoltaic effect in semiconductors to generate electricity directly.

Photovoltaic (PV) panels have been used since the 1950s, but the high cost of solar cell fabrication has limited them to applications such as satellites, off grid installations and mobile devices. However, over the last decade we have seen a tremendous change in the PV market and for the first time solar energy has become price-competitive with fossil fuels. This resulted from large decreases in PV panel costs due to extensive advancements in material science research, improvements in fabrication techniques, and economies of scale. These advancements were driven in part by government subsidies and initiatives, such as the Department of Energy's SunShot Initiative [3], who's goal of reducing utility scale solar power generation from 28 ¢/kWh in 2010 to 6 ¢/kWh by 2020 was met in 2017 (Fig. 1.1). Despite such a drastic reduction in cost, solar energy only made up 1.6% of US power production in 2018 [1]. In order to promote widespread adoption and disrupt the current fossil fuel dominated market, PV panel costs need to be further reduced.

The most common PV devices seen are the traditional single crystal silicon p-n junction panels. They have benefited from the decades of extensive research on silicon's fabrication and material properties, leading to highly efficient and stable solar panels. However, further reductions in its manufacturing cost are difficult do to the energetically demanding processes needed to produce the high quality single crystal silicon necessary for efficient device performance. Due to its poor light absorption properties, thick layers (typically ~300 μm) are needed for sufficient light capture. In order to extract these photo-generated carriers for

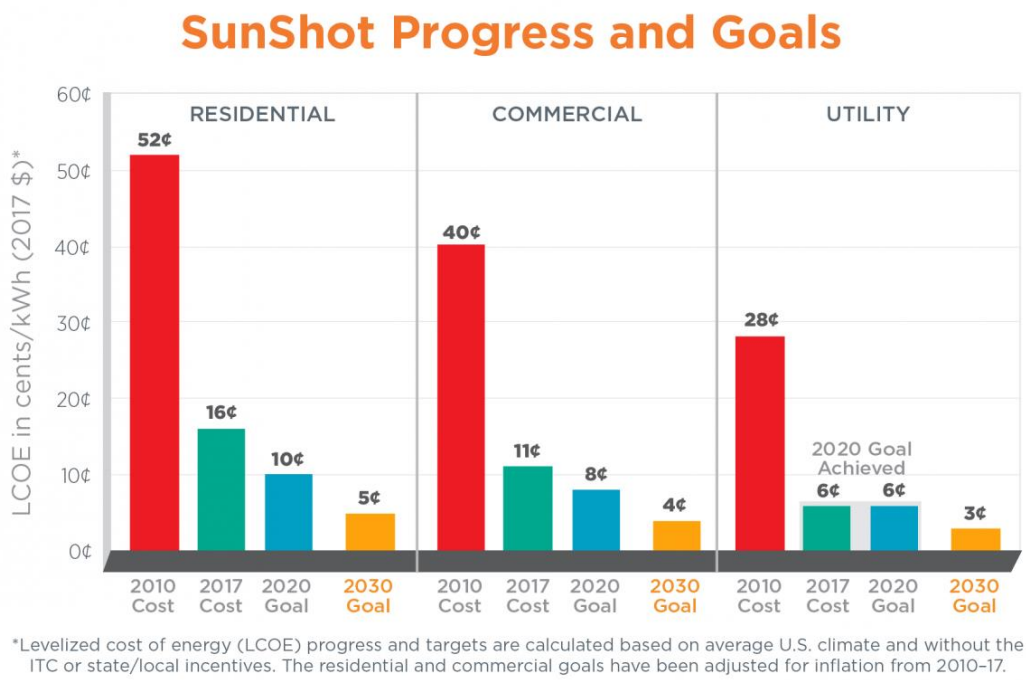

Figure 1.1 SunShot initiative progress and goals [3]. The 2020 goal of achieving 6 ¢/kWh at the utility scale was met in 2017, with the new goal of reaching 3 ¢/kWh by 2030.

electrical use diffusion lengths on the order of the sample thickness are needed. For the thicknesses required in silicon devices, the silicon used has to be very pure and high quality. These prerequisites for efficient silicon devices (thick, high purity/quality) increase panel production costs.

Materials with stronger absorption properties require much thinner absorber layers than traditional crystalline silicon cells, possible reducing production costs, and are used to fabricate "thin film" PV devices. CdTe and $CuIn_{1-x}Ga_xSe_2$ (CIGS) are currently the most popular thin film materials in use with reported device efficiencies of 22.1% and 23.4% respectively [4]. However, concerns about the toxicity of Cd and the scarcity of tellurium and indium limit the viability of the large-scale production of these panels needed to meet the 10's of TW of global

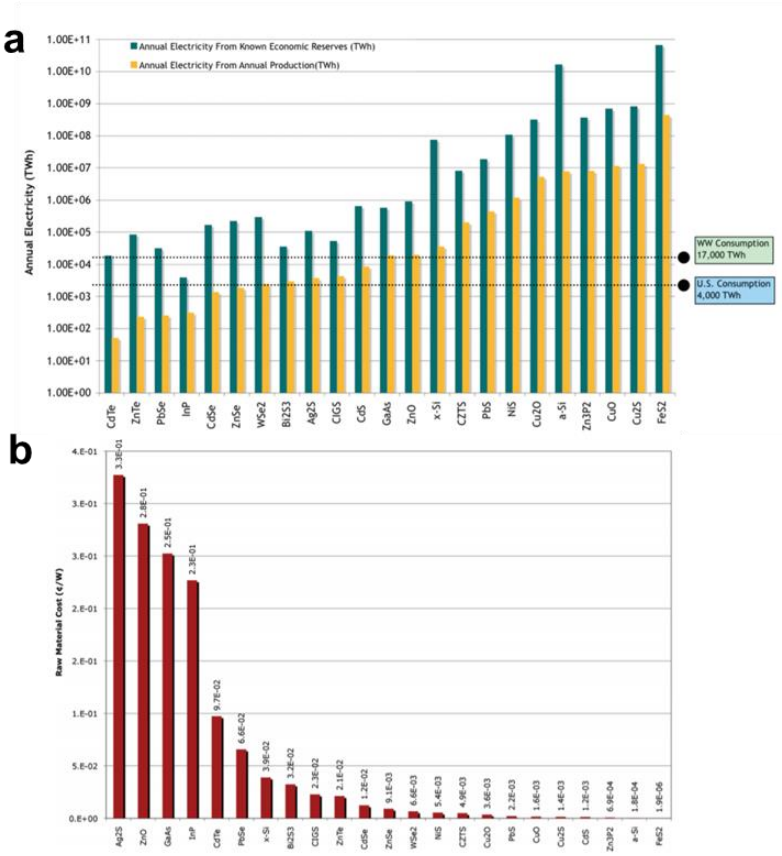

Figure 1.2 Annual potential electricity production and raw material cost for 23 inorganic PV materials. (a) Annual potential electricity production based on known economic reserves (blue) and annual production (yellow). (b) Raw material costs in ¢/W. Images taken from [5].

energy demand. Therefore, we require a thin film material that is cheap, non-toxic, and earth abundant in order to sustain our growth global energy consumption in an environmentally friendly way.

In a 2009 study by Wadia et.al., iron pyrite (FeS_2) was identified as having highest potential for TW-scale solar deployment among 23 inorganic photovoltaic materials [5]. The materials were evaluated on the basis of potential annual power production (determined from reported band gap values and material availability) and materials extraction costs. As can be seen from figure 1.2, iron pyrite (FeS_2) had both the highest potential power production and lowest extraction

costs. Composed of only iron and sulfur, pyrite meets the requirements of cheap, non-toxic, and earth-abundant for an ideal thin film PV material.

1.2 Iron Pyrite (FeS_2)

Iron pyrite (FeS_2), commonly known as fool's gold, forms in a NaCl-like crystal structure ($Pa\bar{3}$), with the Fe^+ ions occupying the Na positions and <111> oriented S-S dimers occupying the Cl positions (Fig. 1.3). The pyrite crystal structure (MX_2) is adopted by many transition metals M and chalcogens X= O, S, Se, Te, including cattierite (CoS_2) and vaesite (NiS_2). FeS_2 also forms a metastable phase, the orthorhombic marcasite. Its formation energy is slightly higher than that of pyrite, therefore it's easily converted by thermal annealing. However, a sulfur-rich environment is necessary during annealing to prevent sulfur loss and the formation of sulfur deficient phases, such as greigite (Fe3S4), smythite (Fe9S11), pyrrhotite (Fe_7S_8) and troilite (FeS).

Research on pyrite started in the mid 1980's due to its potential as an ideal PV material for sustainable, low-cost, TW-scale solar energy conversion. It is composed of earth-abundant, nontoxic, inexpensive elements, has an optical band gap of ~0.95 eV (theoretical maximum efficiency of 30.5% according to the Shockley−Queisser limit with AM 1.5 light, slightly less than the 33.7% limit for an ideal 1.34 eV band gap [6]) and strong light absorption (with an absorption coefficient $\alpha > 10^5$ for $h\nu$ > 1.3 eV) allowing >90% of sun light to be absorbed with only 100 nm thick layers [7]. Additionally, reported room-temperature electron mobility values

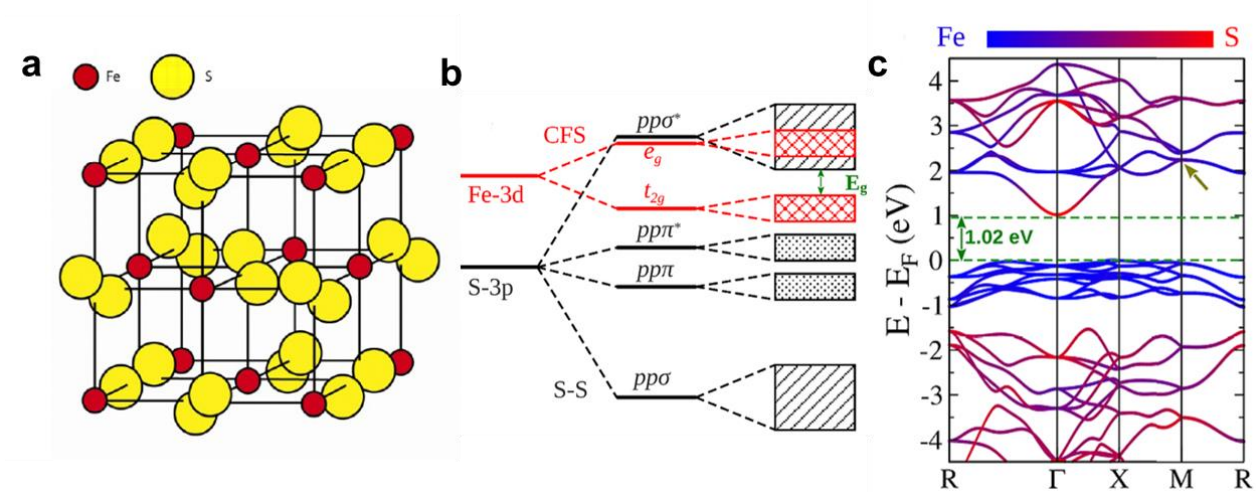

Figure 1.3 Unit cell and band diagrams of iron pyrite. (a) Unit cell of FeS2, adapted from [8]. (b) Schematic band structure derived from atomic Fe and S states. (c) DFT calculated band structure, the color scale indicating Fe and S contributions. (b) and (c) and reproduced from [9].

up to 360 $cm^2V^{-1}s^{-1}$ [10], quantum efficiencies > 90% at 1.26 eV [8], and minority carrier diffusion lengths (100−1000 nm [11,12]) exceeding the thickness needed for complete light absorption make pyrite a truly intriguing material for PV applications.

Despite these appealing properties, pyrite faces three interrelated issues that have so far limited its potential for TW-scale power production. First, pyrite based PV devices suffer from a disappointingly low photovoltage (V_{OC} <200 mV) that limits power conversion efficiencies to < 3% percent [7,13], an order of magnitude lower than the theoretical maximum. Second, pyrite surfaces are rich in electronically active defects that cause Fermi level pinning with strong upward band bending [14,15], surface conduction [16–18], fast recombination [14,19], and the possibility for narrowed surface band gaps [20,21], all of which complicate junction formation [22,23]. Third, the doping of pyrite is poorly understood and poorly controlled, which hinders the progression of fundamental understanding of pyrite and prevents rational device

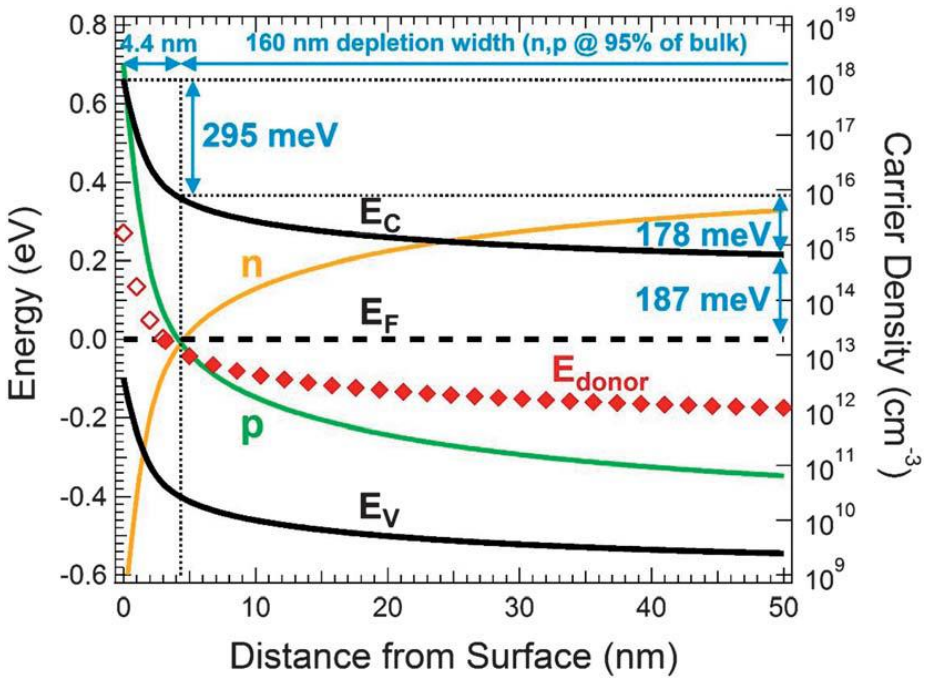

Figure 1.4 Calculated equilibrium band diagram of the pyrite surface at 300 K. Image taken from [16]

engineering [16–18,24,25]. Our lab has demonstrated that high-quality, ultrapure synthetic pyrite single crystals grown by a flux technique feature conductive, *p*-type surfaces (caused by a high density of shallow acceptors pinning the Fermi level near the valance band edge) surrounding interiors made *n*-type by a high concentration of native deep donors [16], while recent work has provided transport evidence indicating sulfur vacancies are responsible for these states [26]. Ionization of these donors near the surface augments the strong electric field of this inversion layer, resulting in a thin triangular potential barrier at the pyrite surface (Fig. 1.4). Following the work of Bronold *et al*. [14], we [16] and then others [19] argued that thermionic-field emission through this triangular surface barrier may be responsible for the large reverse saturation current, poor rectification, and low photovoltage of pyrite devices.

1.3 Scope of This Work

This work utilizes electrical measurements of ultrapure single crystals doped with individual elements in order to gain a better understanding of the electrical effects of controlled doping in pyrite. Chapter 2 gives an overview of the experimental techniques and computational methods used in this work. Chapter 3 further explores the intrinsic properties of our flux grown crystals. In chapter 4 the results of undoped crystals are used as a point of comparison to the properties of flux-grown $Co_xFe_{1-x}S_2$, $Ni_xFe_{1-x}S_2$, and $Cr_xFe_{1-x}S_2$ crystals, in order to establish the basic doping behavior of Co, Ni, and Cr and improving our understanding of the bulk defect chemistry of pyrite.

Chapter 2

Methods

2.1 Single Crystal Synthesis

Iron pyrite single crystals were the basis of these studies. In order to eliminate uncertainty in the results of our experiments, crystal purity and structural quality were of vital importance. The high purity crystals used in these experiments were synthesized via a flux growth technique unique to our lab, first established by Nick Berry and later optimized by Dr. Nima Farhi. This synthesis was first published in [16] and is described in detail below.

2.1.1 Flux Growth

Pyrite singles crystals were formed in a sodium polysulfide flux by heating an evacuated quartz ampule containing a crucible filled with high purity iron, sulfur and sodium sulfide to 780°C and then cooling over a ~24h period. Sodium sulfide was chosen as a flux material do to the low melting point sodium polysulfide has over a wide range of compositions and temperatures (see

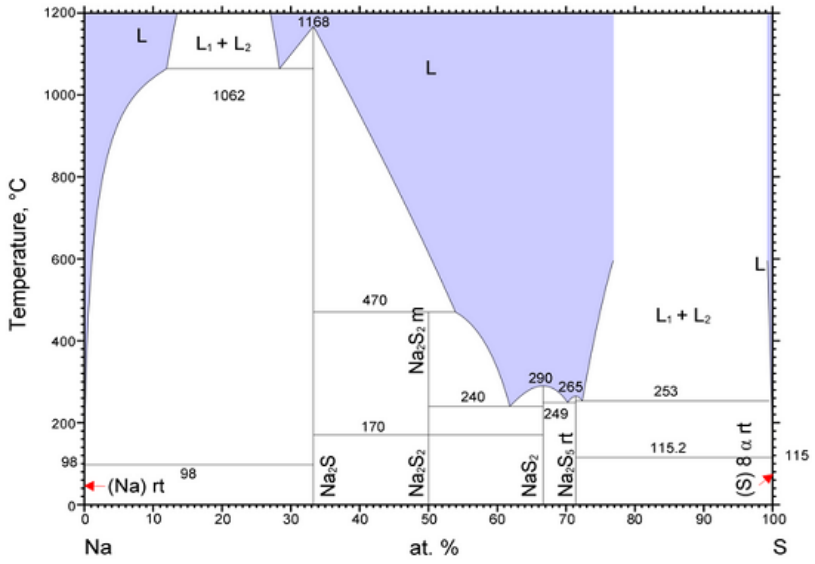

Figure 2.1: Na-S binary phase diagram (data from [27]). The Na-S system has eutectic points as low as 240°C and a large region of binary liquid immiscibility above 253°C near the sulfur-rich end of the system.

fig. 2.1), shares a common anion with pyrite, and has an cation that has been shown to not incorporate into the crystal to any significant degree [16].

Before the synthesis, the high purity precursors are first further purified. Iron powder (99.998%, 22 mesh, Alfa Aesar) is placed into a pyrolytic boron nitride (pBN) crucible and centered in a horizontal tube furnace. The iron was then reduced at 300°C under a flow of 5% H_2/95% Ar for 15 hours in order to remove moisture and any oxides that may have formed. Sulfur powder (99.9995%, Alfa Aesar) was dried and degassed by heating in a quartz round bottom flask at 130°C for 3 hours under vacuum (~30 mTorr). $Na_2S \cdot 9H_2O$ (> 99.99%, Aldrich) was first crushed, then dried and degassed under vacuum (~30 mTorr) at 300°C for 5 hours, resulting a powdered mixture of white NaS_2 and yellow polysulfide. After purification, each precursor's vessel was back filled with Ar, sealed air tight and immediately transferred into a N_2 filled glovebox (< 0.1 ppm O_2). The precursors were then removed from their respective vessels for storage.

While in the glovebox, 0.50 grams of iron powder (8.9 mmol), 0.71 grams of NaS_2 (9.1 mmol), and 1.29 grams of sulfur are loaded into either an alumina crucible (99.5%, LSP Ceramics) or pBN crucible (99.999%, Morgan Technical Ceramics). The crucible is then placed into a half sealed quartz tube. The other end was then attached to a rubber collar with a shut off valve. The collar/quartz tube were brought out of the glovebox and attached to a vacuum system. Before opening the shut off valve to the crucible, the vacuum system was first pumped to <10 mTorr then backfilled with Ar (99.999%). This pump/purge procedure was repeated 3 times. The quartz tube was then evacuated to <10 mTorr and sealed shut with a hydrogen/oxygen torch. The quartz ampule was placed at the center of a vertical furnace, heated to 780°C at a rate of 13°C/min, held at 780°C for 6 hours, cooled to 625°C over 24 hours, then cooled to room temperature naturally (typically ~5 hours). The crucible was then removed from the ampule and placed in a bath of Millipore water for several hours in order to dissolve the NaS_2 flux. The resulting pyrite crystals were sonicated in Millipore water to remove residual flux, further rinsed with Millipore water and then brought into the glovebox for storage.

2.1.2 Doped Single Crystal Growth

Controllably doped crystals were grown in essentially the same manner as described above; the only difference was the addition of the dopant into the crucible after the iron powder, but before the other precursors. Nickel powder (99.996%, 120 mesh, Alfa Aesar), chromium(III) nitrate nonahydrate (99.99%, Aldrich), and octacarbonyldicobalt (stabilized with 1-5% hexane, Alfa Aesar) were used without further purification. To ensure an even distribution the dopants

were added in solution form. We used stock solutions of 0.1M Ni dissolved in hydrazine (98%, anhydrous, Aldrich), 0.1M $Cr(NO_3)_3$ in methanol (99.8%, anhydrous, Aldrich), and 0.1M $Co_2(CO)_8$ in hexane (>99%, anhydrous, Aldrich). The desired amount of solution was diluted with pure solvent to 1 mL total volume and added over the iron. The solvents were then evaporated by heating the crucibles in a box furnace inside the glove box at 200°C for 30 minutes. The rest of the growth procedure is identical to that of the undoped crystals.

2.2 Sample Preparation

2.2.1 Sectioning and Polishing

Many characterization techniques necessitate samples that are relatively thin (such as electrical Van der Pauw measurements) with finely polished, mirror-like surfaces (such as optical transmission or surface science techniques). As such, great care was taken to optimally prepare samples that fit these conditions, resulting in parallel slabs of pyrite that has surfaces with <1 nm RMS roughness (see fig. 2.2).

Most of the crystals used in this study were prepared by first mounting the single crystals in epoxy (Buelher EpoxyCure). A slow-speed saw (Model 650, South Bay Technology) was then used to cut ~700 µm slabs parallel to the largest high quality facet (typically {111} plane, though {210} was seen occasionally). The crystals were then soaked in dichloromethane to dissolve the epoxy. The crystal slabs were polished by mounting the slab onto a metal puck with

Crystalbond™ and sequentially polishing with SiC paper of grit size 600, 800, and 1000, followed by sequential lapping with 3 µm and 1 µm diamond slurries and, finally, lapping with 50 nm Al_2O_3 slurry (Buehler MasterPrep) until no sign of damage is visible under a 5x optical microscope. The crystals were rotated by 90° between each polishing in order to optimally remove damage caused by the previous polishing step. Both sides of the slab were polished in this manner. Residual slurry particles were removed by sonicating in Millipore water. Polished slabs were then stored in the glovebox to reduce oxidation.

Several crystal slabs were instead prepared by using Leica EM TXP. The sample preparation with this tool was nearly identical, except the crystals no longer needed to be mounted in epoxy. Instead, the whole crystal was mounted with the target facet onto a metal chuck mount and the section was cut using diamond saw attachment. This allowed the cut surface to be polished without removing the slab. The surface was then sequentially polished with 9 µm, 5 µm, and 2 µm diamond polishing pads and finally by lapping with a 50 nm Al_2O_3 slurry.

2.2.2 Electrical Contacts

For accurate electrical characterization barrier-less, ohmic, contacts are required. Since contacts to finely polished/as-grown surfaces were often troublesome, ohmic contacts were typically made by carefully scratching the crystal to increase the local surface roughness before applying colloidal silver paste. However, these contacts to Co-containing crystals became non-Ohmic at lower temperatures. To obtain Ohmic contacts to Co-containing samples, 10-20 nm of nickel

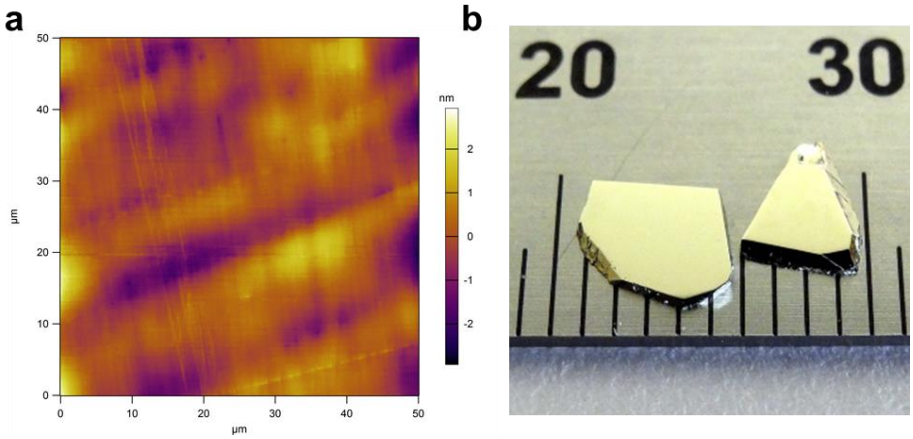

Figure 2.2: Typical pyrite sample preparation. (a) 50 µm x 50 µm AFM topography image of a typical pyrite slab polished surface showing waviness of 1-2 nm and an RMS roughness of 0.64 nm. (b) Photograph of two pyrite slabs. Ruler scale is in mm.

was evaporated onto the roughened corners of the crystal and then covered with colloidal silver paint, even then Co-doped samples became non-Ohmic at sufficiently low temperatures.

2.3 Characterization

To insure our crystals were free from common phase impurities, such as its polymorph marcasite or sulfur deficient phases like pyrrhotite, and elemental contamination their structure and elemental composition were thoroughly characterized.

2.3.1 X-Ray Diffraction (XRD)

Single Crystal XRD data was taken on a performed on a Rigaku SmartLab diffractometer using Cu Kα radiation (λ = 1.5406 Å). X-ray rocking curves and 2Θ-ω scans were acquired on the SmartLab configured with a Ge(440) x 4 monochromator with an angular resolution of 5.4 arcseconds.

Synchrotron XRD measurements were carried out at Beamline 11-BM of the Advanced Photon Source (λ = 0.413141 Å) at Argonne National Laboratory using crushed crystals in capillary transmission mode. Lattice parameters were determined from Rietveld refinement of the XRD patterns (PDXL version 2.6.1.2).

2.3.2 Raman Spectroscopy

Raman spectroscopy was use to further prove disprove the existence of marcasite impurities in our crystals, since it has been shown that Raman is more sensitive in detecting marcasite than regular XRD techniques. Raman spectra were collected using a Renishaw inVia confocal Raman microscope with a 50× objective lens using a 523 nm laser at less than 5 mW. Because of the high light absorption of pyrite limits the probing of this technique to the very surface, samples were powdered right before measurement and scanned in multiple regions to ensure the data acquired was representative of the entire crystal.

2.3.3 Mass Spectrometry

To measure the elemental purity of our single crystals as well as quantify the dopant concentration in doped samples, A Nu AttoM High-Resolution Inductively coupled plasma mass spectrometer (ICP-MS) was used, utilizing the external calibration method. Samples were completely dissolved in double distilled trace metals basis nitric acid (TraceMetal grade, Fisher Scientific) in a Teflon-lined acid digestion vessel (Parr 4744, 45 mL) at 170°C for 4 hours. A multi-element standard (Inorganic Ventures IV-ICPMS-71A) was used to generate standard calibration curves for each element. Cobalt, nickel, and chromium were measured as ^{59}Co, ^{60}Ni, and ^{52}Cr, quantified using the standard calibration curves, and corrected for isotopic abundance to obtain the total concentration of each element in ppm by mass. The results were analyzed using Nu Quant software (version 1.1135.1). Mass concentrations (ppm wt.) were converted to atomic concentrations (ppm at.) using:

$$ppm.at\ of\ x = \frac{\left(\frac{ppm.wt\ of\ x/10^6}{M_x}\right)}{\left(3\times\left(\frac{1}{M_{FeS_2}}\right)+\frac{ppm.wt\ of\ x/10^6}{M_x}\right)}\times 10^6. \qquad (2.1)$$

Where $M_{\mathrm{FeS_2}}$ and M_χ are the molar masses of the stoichiometric FeS_2 and the measured element, respectively. An internal standard (VHG Labs LIS3-100) was used to correct for drift and matrix related artifacts.

Glow discharge mass spectrometry measurements were made on undoped samples by Evens Analytical Group. Powdered pyrite specimens were pressed into high purity In foil (99.99999%) previously cleaned with acid to remove surface impurities. Impurities in the In foil were

analyzed prior to elemental analysis of each sample. Glow discharge conditions of 1.0 kV, 2.0 mA, and 100 Pa of 99.9999% Ar were used for all measurements. Samples were pre-sputtered for five minutes prior to data acquisition. The intensities of the ion beams were measured with a Faraday cup for iron, sulfur and indium isotopes and a Daly conversion detector for all analytes in the samples. The efficiency of the detectors was calibrated using 180Ta (relative isotopic abundance of 0.012%) measured on the Daly detector and 180Ta (relative isotopic abundance of 99.99%) measured on the Faraday cup during analysis of pure Ta metal. Scan points per peak were 70 channels, DAC steps of 7 with integration times of 100 and 160 ms for the Daly detector and Faraday cup, respectively.

2.3.4 Atomic Force Microscopy (AFM)

Surface topography was measured using an Asylum MFP-3D atomic force microscope (AFM) in tapping (AC) mode using AC160TS-R3 (Asylum Research) tips.

2.3.5 Temperature-Dependent Conductivity and Hall Effect

Temperature-dependent conductivity and Hall effect measurement where done inside a glovebox with a modified Ecopia HMS-5000 (0.55 T permanent magnet) using the Van der Pauw method [28]. Due to the unreliable electronics provided with the Ecopia system, our system was modified to use two dual-channel Keithley 2636A SMUs with each channel acting as a

source/sink for each of the 4 contacts in our Van der Pauw geometry, all of which are tied to a common ground. An Arduino Uno is used to control the motor of Ecopia system responsible for moving the permanent magnets used for Hall effect measurements. A Lakeshore Cryotronics 321 temperature control unit is used to monitor and control the stage temperature. The system is operated/automated with a homemade LabView program (see fig. 2.3).

The Hall coefficient was calculated as $R_{\mathrm{H}} = \frac{V_{\mathrm{H}} d}{IB}$, where V_{H} is the averaged Hall voltage measured, d the crystal thickness, I the applied current, and B the magnetic field strength. The Hall voltage is an average of the values measured for both magnetic field directions and perpendicular sample diagonals. Current reversal was used to eliminate Ohmic voltage drops due to misaligned contacts when measuring Hall voltages. The applied current ranged from 1 μA at 80 K to 1-2 mA at 350 K for undoped and Ni- and Cr-containing crystals. The high conductivity of Co-doped crystals required higher currents. The quality of the data was checked by ensuring <5% difference in voltage readings upon current reversal for conductivity values and <10% difference in Hall coefficient values for perpendicular directions. Carrier concentrations and mobilities were calculated using the single carrier approximation.

Samples are mounted with thermal grease (Apiezon Type N) to glass slides bonded to the sample stage. Ohmic contacts were confirmed by ensuring linear IV curves between all contacts.

2.4 Data Modeling

To help interpret our experimental data, modeling and density function theory calculations were utilized. The specifics of these calculations are detailed below.

2.4.1 Charge Transport

In order to accurately replicate our electrical data a multilayer conduction model needed to be utilized. This conduction model was pioneered by Petritz [29] and first applied to the conduction in pyrite by Dr. Moritz Limpinsel [16]. The crux of the model assumes that conduction in our samples happens in three parallel layers; the n-type bulk and two identical p-type surface layers (see Fig. 2.3).

Here we calculate the carrier concentrations (n and p), conductivity (σ), and Hall coefficient (R_H) of each layer by using the charge neutrality condition

$$N_D^+ + p = N_A^- + n. \tag{2.4}$$

Where N_D^+ and N_A^- are the concentrations of ionized donors and acceptors, given by [30]

$$N_D^+ = \frac{N_D}{1 + e^{\frac{(E_F(T) - E_D)}{k_b T}}} \tag{2.5}$$

and

$$N_A^- = \frac{N_A}{1+ e^{\frac{(E_A - E_F(T))}{k_b T}}} \tag{2.6}$$

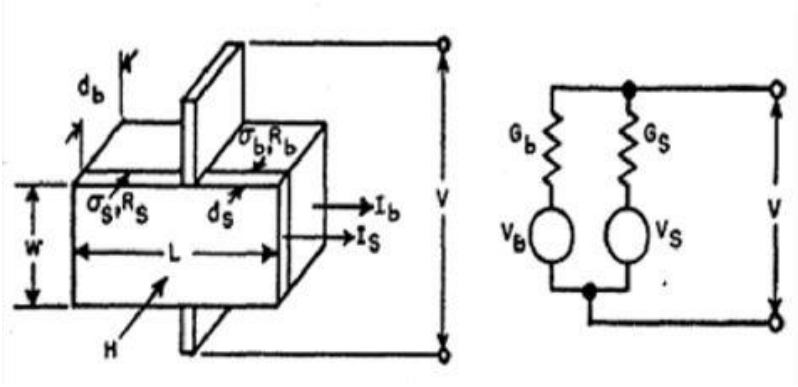

Figure 2.3: Conductivity and Hall effect of a multilayer system established by Petritz. The subscripts s and b denoted properties of the surface and bulk respectively. Image taken from [29].

respectively. Where here N_D and N_A are the concentration of donors and acceptors and E_D and E_A are their respective energies. The carrier concentrations n and p are given by

$$n = \int_{E_C}^{\infty} DOS(E) \left(\frac{1}{e^{\frac{E - E_F(T)}{k_b T}} + 1} \right) dE \tag{2.7}$$

and

$$p = \int_{-\infty}^{E_V} DOS(E) \left(1 - \frac{1}{e^{\frac{E - E_F(T)}{k_b T}} + 1} \right) dE. \tag{2.8}$$

In this work we assume the a parabolic DOS. The fits worked by self-consistently solving for the temperature dependent Fermi level $E_F(T)$. This was done by inserting eqn. (2.5) through (2.8) into eqn. (2.4) and solving for E_F at each temperature. Using $E_F(T)$ we solved for n(T) and p(T), from which we can then calculate σ(T) and $R_H(T)$ from the generalized expressions:

$$\sigma = e(p\mu_h - n\mu_e) \tag{2.9}$$

and

$$R_H = \frac{p\mu_h^2 - n\mu_e^2}{e(p\mu_h - n\mu_e)}. \tag{2.10}$$

The overall sample properties were then calculated by combining the bulk and surface contributions using [29]

$$\sigma_{total} = \sigma_b \frac{d_b}{d} + 2\sigma_s \frac{d_s}{d} \tag{2.11}$$

and

$$R_{H,total} = R_{H,b}\left(\frac{\sigma_b}{\sigma_{total}}\right)^2 + 2R_{H,s}\left(\frac{\sigma_s}{\sigma_{total}}\right)^2, \tag{2.12}$$

where d_b and d_s are the thicknesses of the bulk and surface layers and $d = d_b + 2d_s$ is the total sample thickness. For this work, the bulk and surface layers were assumed to be uncompensated n and p-type materials, respectively. The bulk electron mobility $\mu_{e,b}$ was determined from fits to the unipolar region of the Hall data, while the surface hole mobility $\mu_{h,s}$ was parameterized from thin film mobilities. Therefore this routine uses 5 free fit parameters ($N_{A,s}$, $N_{D,b}$, $E_{A,s}$, $E_{D,b}$, and $\mu_{-e,b}$)

Chapter 3

Undoped Single Crystals

3.1 Characterization

To explore the intrinsic properties of iron pyrite it is important to start with the highest purity and crystallographically perfect crystals as possible. The flux growth method (described in sec. 2.2.1) pioneered by Nick Berry and optimized by Dr. Nima Farhi provided crystals that met these conditions. In the following sections the structural, elemental, and electrical properties of these single crystals is presented. The results shown in this chapter fully characterize these crystals and make a great reference point for the effects of the controlled doping explored in chapter 4.

3.1.1 Elemental Characterization

The elemental purity of our undoped crystals has been reported before showing a purity of 99.998% on a metals basis with the only elements above 1 ppm being Cr (6.4 ppm), B (6.3ppm), Si (4.2pm), Na (4.2 ppm), and Cl (1.1 ppm) [16]. In this study elemental purity was determined by high-resolution inductively coupled plasma mass spectrometry (HR-ICP-MS). We used a

combination of multi-element standards and semi-quantitative analysis to estimate the concentrations of 61 elements, 40 elements quantitatively and 21 elements semi-quantitatively (see sec. 2.3.3). We note that a small number of relevant elements were not measured with ICP-MS, including the light elements (H, Li, Be, B), the gas formers (C, N, O), the halogens, and a few others due to contamination of the shared instrument (Ca, Al, Si, P). Table 3.1 summarizes the results for a typical sample. The major contaminates seen are Na (26.7 ppm), Cr (3.1 ppm), Mn (0.2 ppm), Ni (0.4 ppm), Cu (0.4 ppm), Zn (4.1 ppm), and Se (0.2 ppm), while all other measured elements were in negligible concentrations. The sodium concentration varies widely from 1-1000 ppm depending on how thoroughly a given sample is rinsed in water prior to digestion for ICP-MS analysis. We previously showed that sodium exists as a surface residue from the Na_2S-based flux rather than a lattice impurity [16], so we ignore its presence here. On the basis of the ICP-MS results, we conclude that the undoped crystals have a typical impurity concentration of 8.3 ppm of the elements measured. Cu, Zn, and Se were not reported as contaminates in our previous publication because their concentration is below the detection limit of the GDMS measurement. They, along with Ni, are listed as measured impurities of our sulfur precursor, although their concentration is surprisingly high in our samples if this is the only source of these elements. Cr and Mn likely originate from our Fe precursor. The S:Fe ratio was measured, with results in the 1.972 – 1.985 range. These results deviate from the ideal 2:1 ratio likely because of sulfur loss during the sample digestion process.

Glow discharge mass spectrometry (GDMS) measurements from Li - U were conducted on undoped samples in order to look at some of the elements we didn't have access to by ICP-MS. Results were similar to those previously published, with the major impurities not reported by

Undoped Single Crystal			
S:Fe = 1.98138[b]			
element	ppm at.	element	ppm at.
Na	26.7362	Te[a]	0.0078
Mg	0.0410	Cs	<0.0005
Sc	0.0353	Ba	<0.0364
Ti	0.0444	La	0.0001
V	0.0587	Ce	0.0003
Cr	3.0655	Pr[a]	<0.0002
Mn	0.1995	Nd	<0.0006
Co	0.0321	Sm	0.0002
Ni	0.4413	Eu	0.0002
Cu	0.3614	Gd	<0.03
Zn	4.1077	Tb	0.0012
Ga	<0.0023	Dy	<0.0004
Ge	0.0025	Ho	<0.0002
As	0.0133	Er	<0.0003
Se	0.1388	Tm	<0.0003
Rb	0.0012	Yb	<0.0004
Sr	0.0045	Lu	0.0018
Y[a]	<0.0034	Hf[a]	0.0001
Zr[a]	0.0033	Ta[a]	<0.0001
Nb[a]	0.0002	W[a]	<0.0011
Mo[a]	0.0031	Re[a]	0.0000
Ru[a]	0.0394	Os[a]	0.0003
Rh[a]	0.0097	Ir[a]	0.0001
Pd[a]	0.0075	Pt[a]	0.0153
Ag	<0.005	Au[a]	<0.0015
Cd	0.0001	Hg[a]	<0.3
In	0.0050	Tl	<0.00005
Sn[a]	0.0034	Pb	0.0817
Sb[a]	0.0002	Bi	<0.0040
		U	<0.0008

Table 3.1: ICP-MS results of a typical undoped single crystal pyrite reported in atomic ppm. [a] Elemental concentration determined by semi-quantitative methods. [b] Due to sulfur loss during sample preparation, the measured S:Fe deviates from the expected 2:1.

ICP-MS being B (1.1 ppm), Al (0.6 ppm), Cl (4.5 ppm), and Ca (1.1 ppm). In combination with the ICP-MS results this leads to a total impurity concentration, ignoring Na, of ∼16 ppm. Our halogen-free flux synthesis leads to a low concentration of halides in our samples, in contrast to the relatively high levels of halides often present in CVT-grown pyrite crystals. The electronic activity of halide impurities in pyrite remains an open question. Of the elements we were unable to measure (H, C, N, O), we believe that only hydrogen and oxygen are important impurities that could be present in significant concentration. Most importantly for the work described in chapter 4, we find the average Cr, Co, and Ni concentration to be 4.4 ppm, < 0.36 ppm, and 0.84 ppm respectively in our undoped samples.

3.1.2 Structural and Elemental Characterization

Our double-side polished slabs have irregular shapes up to 6 mm on a side (Fig. 2.2b), mis-cut angles of <6° off the (111), and good co-planarity of the front and back surfaces (to <2°). AFM topography scans of 50×50 μm regions of the polished surfaces show a long-wavelength surface waviness of 1-2 nm amplitude and a typical rms surface roughness of <1 nm (Fig. 2.2a).

X-ray diffraction (XRD) scans show that the slabs are highly-perfect, phase-pure pyrite crystals. A vast majority of the crystals discussed in this thesis have a (111) orientation (Fig. 3.1a), though we occasionally see (210) oriented facets. XRD rocking curve measurements were used to determine the crystallographic quality of our single crystals. Figure 3.1b shows a peak width of 6.5 arcseconds indicating excellent structural perfection even after polishing. As a reference,

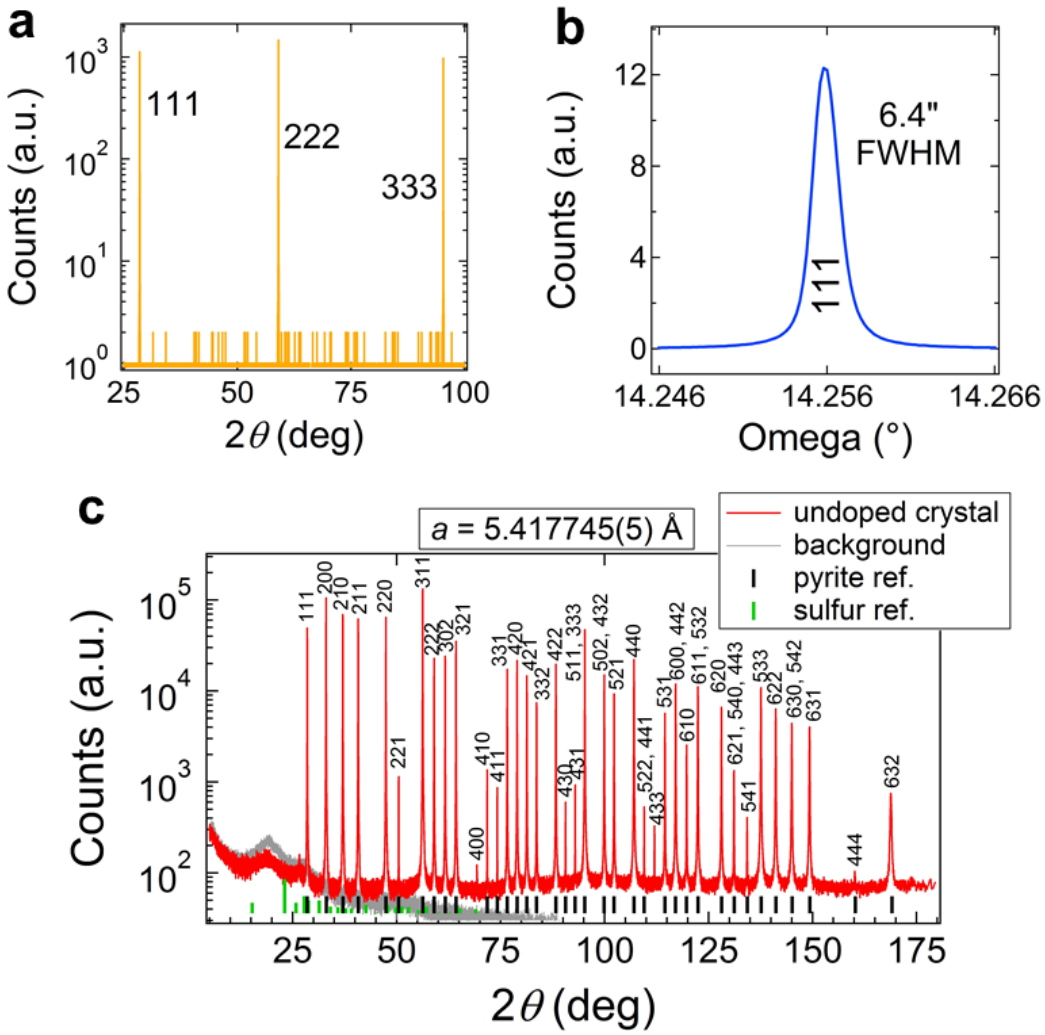

Figure 3.1: Structural characterization of undoped pyrite crystals**.** (a) 2*Θ*–*ω* XRD scan of a polished (111)-oriented pyrite single crystal slab on a log scale. (b) (111) rocking curve of a pyrite slab, showing a FWHM of 6.4 arcseconds. (c) Synchrotron XRD pattern of a powderized crystal on a log scale. All reflections index to pyrite FeS_2 (PDF# 00-042-1340) with the exception of the tiny peak at 26.6°. This peak is caused by residual flux and eliminated by rinsing the sample with water. Rietveld refinement of the data gives a cubic lattice parameter of 5.417745(5) Å at room temperature. The background pattern is of an empty capillary tube. Black and green bars denote the reference patterns for pyrite and orthorhombic sulfur, respectively.

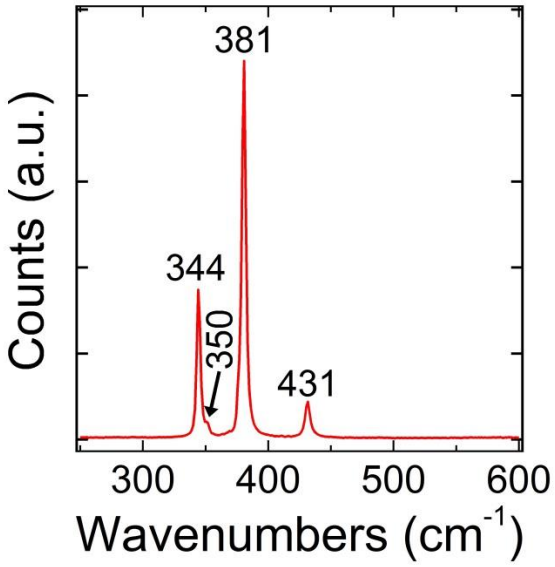

Figure 3.2: Raman spectra of a powderized single crystal showing the dominant bands of pyrite at ~344 cm^{-1} and ~381 cm^{-1}, a small shoulder at ~350 cm^{-1}, and a minor band at ~431 cm^{-1}, corresponding to the Ag (S2 dumbbell libration), E_g (S2 dumbbell stretching), $T_g(1)$, and $T_g(3)$ vibrational modes, respectively. The marcasite peak typically seen at ~320 cm^{-1} is absent.

a commercial prime grade CZ-grown Si wafer had a peak width of 8.5 arcseconds. Synchrotron powder XRD is consistent with phase-pure pyrite, with no evidence for crystalline or amorphous impurities (Fig. 3.1c). We calculate a cubic lattice constant of 5.417745(5) Å from Rietveld refinement of the XRD data.

Raman spectroscopy was used as a complimentary technique to XRD to check for the presence of marcasite, a polymorph of pyrite, since it has been shown that Raman is more sensitive to in detecting marcasite than other XRD techniques. Because of the strong light absorption of pyrite, the probe depth of Raman is limited to the near surface. In an attempt to get data representative of the entire crystal, samples were powderized immediately before measurement and spectra were taken in several locations. We observed a total of four separate Raman bands from pyrite (Fig. 3.2): dominant bands at ~344 cm^{-1} and ~381 cm^{-1}, a small

shoulder at ~350 cm^{-1}, and a minor band at ~431 cm^{-1}, corresponding to the A_g (S2 dumbbell libation), E_g (S2 dumbbell stretching), $T_g(1)$, and $T_g(3)$ vibrational modes, respectively. Notably the spectra is absent of the major marcasite band seen at ~315-325 cm^{-1}.

3.1.2 Hall Effect Studies

Undoped crystals were characterized by variable-temperature Hall effect, electrical conductivity (Figure 3.3). The electrical behavior of these crystals is essentially the same as described in our previous report [16], where a thin, conductive, hole-rich (*p*-type) layer at the surface of the *n*-type pyrite crystals progressively dominates transport as bulk electrons freeze out to deep donors with decreasing temperature. This transition from bulk to surface conduction manifests as a non-monotonic Hall coefficient (R_H) that is unambiguously negative at higher temperature (indicating *n*-type conduction), a minimum at ~140 K (depending on crystal thickness), and noisy but often positive below ~100 K (Fig. 3.3a). Good fits to the experimental data (dashed lines in Fig. 2) can be obtained using a multi-layer transport model (see sec. 2.6.1) that assumes parallel conduction via a thick bulk *n*-type layer with a high concentration of deep donors ($N_{D,bulk}$ = 10^{18}-10^{19} cm^{-3}, E_C - E_D = 380-400 meV) and a ~4 nm thick *p*-type surface layer on both sides of the crystal with a high concentration of shallow acceptors ($N_{A,surface}$ = 10^{20}-10^{21} cm^{-3}, E_A - E_v = 30-50 meV). Transport is unipolar *n*-type above ~150K, with a typical electron density (*n*) and mobility (μ_e) of 2 × 10^{15} cm^{-3} and 300 cm^2 V^{-1} s^{-1} at 300 K (Fig. 3.3b-c, Table 3.2 for exact fit results). This carrier density is about 10^3 larger than the predicted intrinsic carrier concentration

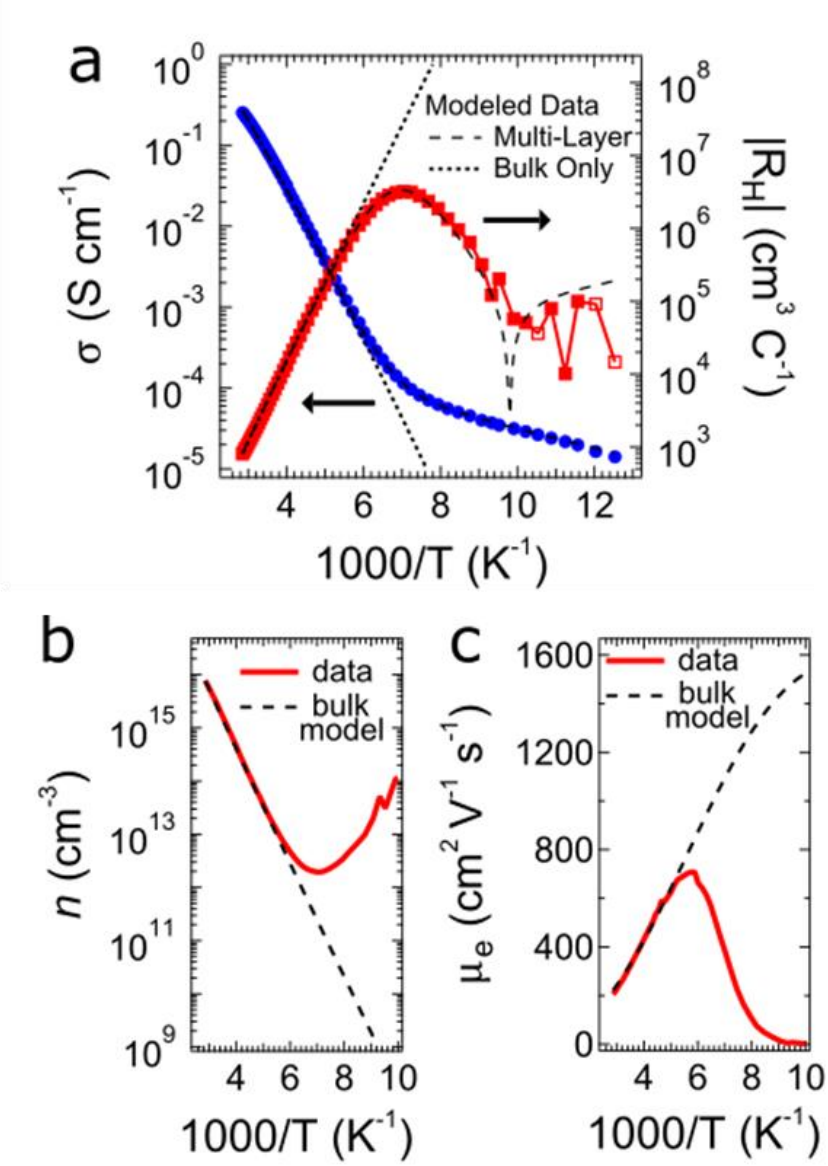

Figure 3.3: Electrical properties of undoped pyrite crystals. (a) Conductivity and absolute Hall coefficient versus inverse temperature for a typical sample (590 μm thick). Closed (open) squares represent negative (positive) values of R_H. Dashed lines are fits to the data using a multi-layer conduction model [16]. (b) Electron density (n) and (c) mobility (μ_e) from 100-350 K. Solid lines are derived from the experimental data by assuming a unipolar Hall coefficient (i.e., $R_H = -1/ne$). Dashed lines are results from the model showing the behavior of the bulk electrons. The unipolar approximation ($n\mu_e^2 \gg p\mu_h^2$) is satisfied only at temperatures where the two traces overlap.

Parameter (unit)	Fit Results
N_D (cm^{-3})	3.16×10^{18}
$E_C - E_D$ (meV)	400
N_A (cm^{-3})	5.01×10^{20}
$E_A - E_V$ (meV)	35
μ_e ($cm^2\ V^{-1}\ s^{-1}$)	297
μ_h ($cm^2\ V^{-1}\ s^{-1}$)	3
d_s (nm)	4.4

Table 3.2: Fit parameters used in Figure 3.3.

of pyrite ($n_i \sim 10^{12}$ cm^{-3}). Below 150 K, the samples first enter a regime of mixed conduction (where both bulk electrons and surface holes contribute substantially to the current), followed by dominant *p*-type surface conduction at lower temperatures. The origin of the unintentional *n*-type doping of bulk pyrite is not understood, but sulfur vacancies (V_S) that act as deep donors are a leading suspect [7,16] and recent reports have shown good evidence of this [26]. The *p*-type surface layer also remains somewhat mysterious, but probably results from intrinsic surface states that pin the Fermi level near the valence band edge, causing surface inversion in nominally-undoped samples [15,16,18,31].

Chapter 4

Doped Iron Pyrite Single Crystals

While the surface inversion layer continues to be a leading issue in realizing pyrite as a solar absorbing layer in photovoltaic devices, the poorly understood and poorly controlled doping of pyrite both prevents rational device engineering [16–18,24,25] and hinders the progression of the fundamental understanding of pyrite. The impact of important fundamental studies of pyrite and its surface are often diminished due to the use of natural crystals or low purity precursors, without first considering the concentration and effect of impurities on the properties of pyrite. Given the high quality and purity, our flux-grown crystals provide a suitable experimental platform for doping studies. In this paper, we report on the properties of flux-grown $Co_xFe_{1-x}S_2$, $Ni_xFe_{1-x}S_2$, and $Cr_xFe_{1-x}S_2$ crystals in the dilute doping limit ($x < 0.01$, equivalent to < 3300 ppm at.), with the goals of establishing the basic doping behavior of Co, Ni, and Cr and improving our understanding of the bulk defect chemistry of pyrite in order to engineer high-performance pyrite devices.

$Co_xFe_{1-x}S_2$ and $Ni_xFe_{1-x}S_2$ alloys have been studied for many years due to their interesting electrical and magnetic properties and relevance to spintronics. CoS_2 and NiS_2 are members of the pyrite family of metal disulfides (MS_2, with M = Mn-Zn). Several groups have reported on

the behavior of dilute Co and Ni (< 500 ppm) in natural or CVT-grown iron pyrite crystals. In important early work, Chandler and Bené concluded from low-temperature EPR data of single crystals grown by vapor transport with Cl_2 that cobalt on an iron site (Co_{Fe}) is a very shallow donor and nickel on an iron site (Ni_{Fe}) is a very deep donor near the middle of the band gap [32]. EPR spectra of $Co_xFe_{1-x}S_2$ crystals acquired at 2-4 K (in an effort to freeze out the itinerant cobalt electrons) showed the presence of low-spin Co^{2+} (^2E_g ground state), the onset of semi-metallic behavior at $x \approx 0.0001$ ([Co] = 30 ppm), and metallic conduction for $x \geq 0.005$ (1600 ppm). Spectra of $Ni_xFe_{1-x}S_2$ crystals at 77 K showed the presence of Ni^{2+} ($^3A_{2g}$ ground state) with fully localized e_g electrons. These authors noted some delocalization of the Ni e_g electrons in a narrow defect band at higher Ni concentrations (650-10,000 ppm). In several papers investigating $Ni_xFe_{1-x}S_2$ alloys made by ICl_3 transport, Ho *et al*. argued that Ni_{Fe} is actually a fairly good donor in pyrite, contrary to the EPR results [33,34]. Savage *et al*. studied natural single crystals using room-temperature Hall effect and conductivity measurements and concluded that Co impurities increase the free electron concentration but Ni impurities do not [35], confirming previous conclusions by Lehner *et al*. on polycrystalline samples grown by CVT from low-purity (99-99.9%) starting materials [36]. Earlier transport measurements had indicated degenerate *n*-type conduction in Co-doped CVT crystals [37,38] and thin films [39]. More recently, very detailed magnetization and transport studies by Guo *et al*. showed that $Co_xFe_{1-x}S_2$ crystals grown by I_2 transport are metallic for x at least as small as 0.0003 ([Co] ≈ 100 ppm) [40,41]. These authors found that the Co_{Fe} donor efficiency (the increase in carrier concentration per unit increase in Co concentration) may be close to unity at low [Co] ($x <$ 0.004, 1300 ppm) but drops rapidly with increasing [Co] to a value of ~0.1 at $x = 0.075$ (25,000

ppm), suggesting a concentration-dependent degree of localization of the Co e_g electrons. Magnetic cluster formation was reported at temperatures below 10 K in samples with low [Co] and above the Curie temperature in samples with $x \geq 0.007$ (2333 ppm).

Here, we combine variable-temperature electrical, optical, and magnetic measurements with DFT calculations to carefully study the impact of substitutional cobalt, nickel, and chromium on the properties of ultrapure pyrite crystals. These three transition elements are common impurities in natural pyrite crystals and either known (Co) or suspected (Ni and Cr) *n*-type dopants. Lehner *et al*. recently used room-temperature optical transmission spectroscopy to estimate the energies of the defect levels introduced by high concentrations of Co or Ni in pyrite single crystals grown by $FeBr_3$ transport [25]. Our study extends past work to higher-purity pyrite host crystals that enable clearer elucidation of composition-property relationships. We also focus on a range of lower impurity concentrations (<1000 ppm) that is more relevant to the electronic doping of semiconductors. By correlating electrical, optical, and magnetic data acquired as a function of impurity concentration, sample thickness, and temperature with insights from DFT models, a detailed and self-consistent picture of the defect energy levels, concentrations, and charge states can be established. Using this approach, we show that Co is a creates a state within the pyrite conduction band with a high donor efficiency at low doping concentrations and essentially zero magnetic moment for [Co] < 350 ppm, making it an ideal *n*-type dopant for pyrite. We also present the first doping and transport measurements of $Cr_xFe_{1-x}S_2$ crystals. Chromium is less studied than Co and Ni because it does not crystallize in the pyrite structure.

4.1 Cobalt Doped ($Co_xFe_{1-x}S_2$)

Cobalt was added to the crystal synthesis in the form of dicobalt octacarbonyl (DOC) dissolved in hexane. The solution was added to the iron in the crucible via a micro pipette then heated to 200°C for 30 minutes to evaporate the hexane, with the rest of the synthesis proceeding as the undoped crystals (sec. 2.1.1). Adding the dopant in solution phase allowed us a high degree of control in the concentration of dopants added as well as helped ensure the dopant was incorporated homogeneously. DOC was chosen rather than dissolving Co in nitric acid in order to avoid unintentional nitrogen and oxygen contamination in our crystals. We made crystals with cobalt concentrations [Co] of 5-5580 ppm (atomic basis), below are the properties investigated in these intentional Co doped pyrite single crystals.

Sample	Section*	[Co] (ppm at.)	Average [Co] (atoms/cm^{-3})	*X*
1	1a	244	2.0×10^{19}	0.00082
	1b	224		
	2a	300		
	2b	316		
2	1a	253	2.2×10^{19}	0.00087
	1b	261		
	2a	330		
	2b	283		
	3a	309		

Table 4.1: [Co] uniformity in $Co_xFe_{1-x}S_2$ crystals.* Section 1 refers to the top of the crystal and section 3 to the bottom of the crystal (a and b refer to pieces of the crystal in the same z-section, measured to check for homogeneity in the xy plane).

4.1.1 Elemental Characterization

ICP-MS measurements were used to quantify the concentration of Co incorporated into our crystals. In order to test the homogeneity of Co, crystals were sectioned into several slabs parallel to the top facet and each slab was fractured into two pieces before each was dissolved in acid and each measured by ICP-MS separately. By breaking up the crystal in this manner we were able to check the uniformity of Co in our samples. Table 4.1 shows the results of two such crystals, displaying no significant inhomogeneity in our samples. The small variation seen likely arose from errors in the ICP-MS measurement of solution preparation. While the cobalt was readily incorporated into the crystals using this approach, we saw insignificant changes in the concentrations of most other measured elements (see Table 4.2). The only element we see increase to over 1 ppm is Cu, which is a likely a surface contaminate from the slow speed saw used during the sectioning of this crystal before measurement.

333 ppm Co Sample			
S:Fe = 2.060193262			
element	**ppm at**	**element**	**ppm at**
Na	299.8575	Te[a]	0.1070
Mg	0.8903	Cs	0.0007
Sc	0.0593	Ba	0.0153
Ti	0.0948	La	0.0008
V	0.0309	Ce	0.0006
Cr	2.4847	Pr[a]	0.0067
Mn	0.0860	Nd	0.0364
Co	333.1991	Sm	0.0098
Ni	1.5212	Eu	0.0028
Cu	1.2066	Gd	0.0053
Zn	2.6183	Tb	0.0017
Ga	<0.063	Dy	0.0045
Ge	0.0028	Ho	0.0010
As	0.0701	Er	0.0038
Se	0.3193	Tm	0.0005
Rb	0.0049	Yb	0.0055
Sr	0.2997	Lu	0.0024
Y[a]	0.0024	Hf[a]	0.0035
Zr[a]	0.0023	Ta[a]	0.0010
Nb[a]	0.0023	W[a]	0.0126
Mo[a]	0.0187	Re[a]	0.0028
Ru[a]	0.0374	Os[a]	0.01491
Rh[a]	0.0194	Ir[a]	0.00164
Pd[a]	0.0336	Pt[a]	0.0108
Ag	0.1948	Au[a]	0.0160
Cd	0.0374	Hg[a]	0.2932
In	0.0085	Tl	0.0027
Sn[a]	0.0088	Pb	0.0760
Sb[a]	<0.03	Bi	0.0070
		U	0.2648

Table 4.2: ICP-MS results of a typical Co-doped crystal ([Co] = 333 ppm) pyrite reported in atomic ppm.
[a] Elemental concentration determined by semi-quantitative methods.

4.1.2 Structural Characterization

Crystals grown with this cobalt precursor show similar size, shape, faceting, and quality as undoped crystals. High-resolution synchrotron powder XRD showed no evidence of phases other than pyrite, even for crystals with the highest cobalt concentration studied here (5580 ppm, Fig. 4.1). These observations are reasonable given that FeS_2 and CoS_2 (cattierite) form a solid solution over the entire compositional range [42,43]. Unit cell length was determined for undoped and doped crystals by Rietveld refinement of the XRD patterns. We observed shifts in XRD peak positions that are consistent with lattice expansion as well as an increased unit cell length due to the incorporation of cobalt, in rough agreement with Vegard's law (a = 5.524 Å for CoS_2) [44] and the expectation that cobalt occupies iron sites in the pyrite FeS_2 structure to form substitutional Co_{Fe} defects [41].

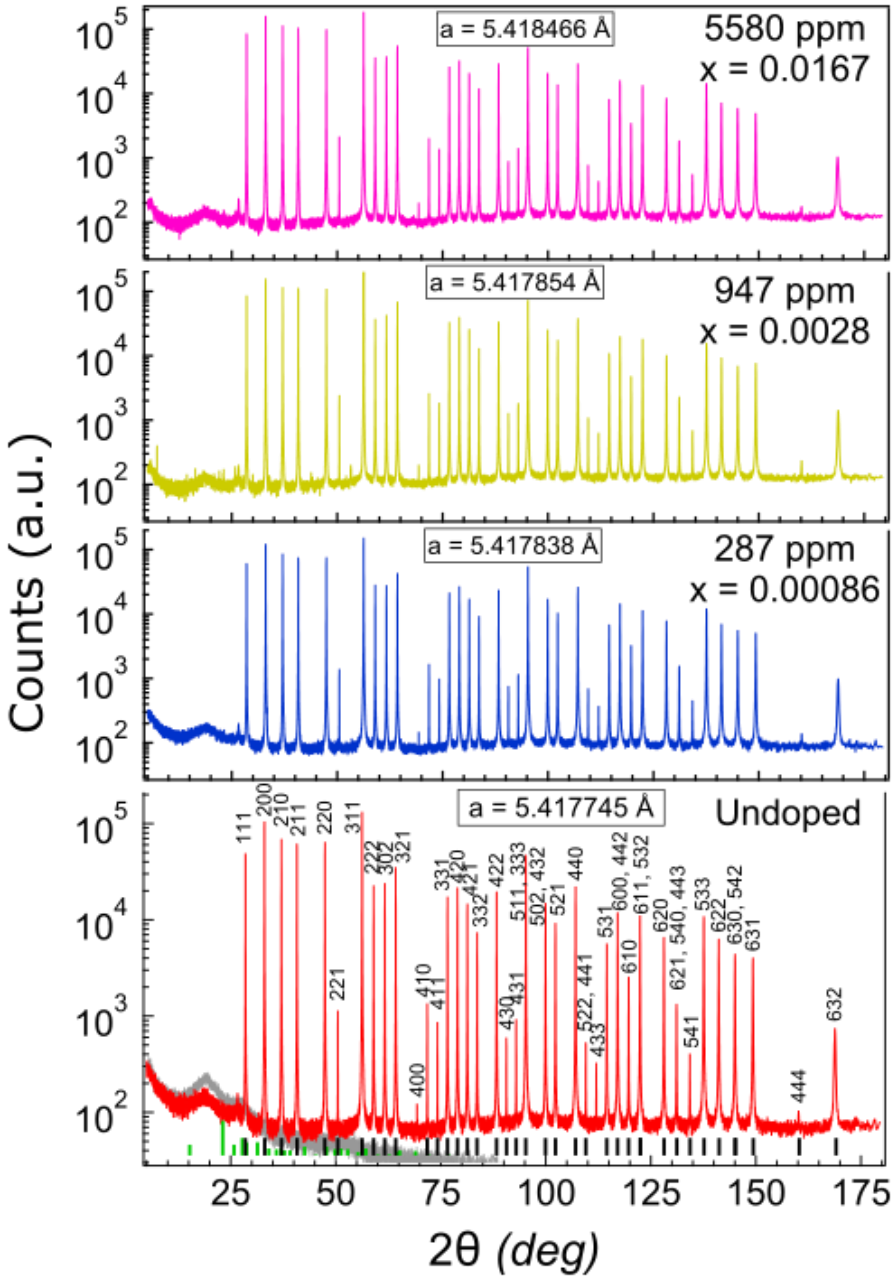

Figure 4.1. Synchrotron XRD pattern of a powdered undoped and powdered $Co_xFe_{1-x}S_2$ crystals with x = 0.00086, 0.0028, and 0.0167, presented on a log scale. All 39 reflections index to pyrite and no other phases are detected. Lattice parameters were calculated by Rietveld refinement with PDXL2 software at room temperature. The background pattern is for an empty capillary tube. Overlaid on the undoped data are a background pattern of an empty capillary tube (gray) as well as reference patterns for pyrite (black bars) and orthorhombic sulfur (green bars).

4.1.3 Hall Effect Studies

Variable-temperature electrical conductivity and Hall coefficient data (Figure 4) show that cobalt induces metallic behavior in pyrite, in agreement with previous reports on the electrical properties of $Co_xFe_{1-x}S_2$ crystals [25,32,40]. The free electron density and conductivity both increase, while the electron mobility decreases, with increasing cobalt concentration (Fig. 4.2a-c). At Co concentrations as low as 5ppm (3.7×10^{17} cm^{-3}) we observe decreasing conductivity with increasing temperature and a mobility temperature dependence proportional to T^{α}, with $\alpha \approx -1.7 \pm 0.2$. This is close to the $T^{-3/2}$ expected for the thermally activated phonon scattering that is typical of conduction in metals. This behavior, along with a temperature independent carrier concentration, indicates metallic conduction in even our most lightly doped samples. Along with our magnetic measurements presented below, we could conclude that Co creates a defect state, E_D, resonant with the conduction band states of pyrite, i.e. that E_D lies above the conduction band minimum (CBM), E_C, such that $(E_D-E_C) > 0$. However, we find that only ~60% of cobalt incorporated results in additional free carriers for low doping concentrations (3-100ppm) and that this value further decreases when additional Co is added to the system, down to ~28% for our largest Co concentration measured (1812ppm). From this, there appears to be a concentration dependent compensating defect state created with Co incorporation. The larger decrease in additional free carriers for greater doping concentrations could also be explained by the reduction in ionization efficiency for increasingly doped degenerate semiconductors [45,46].

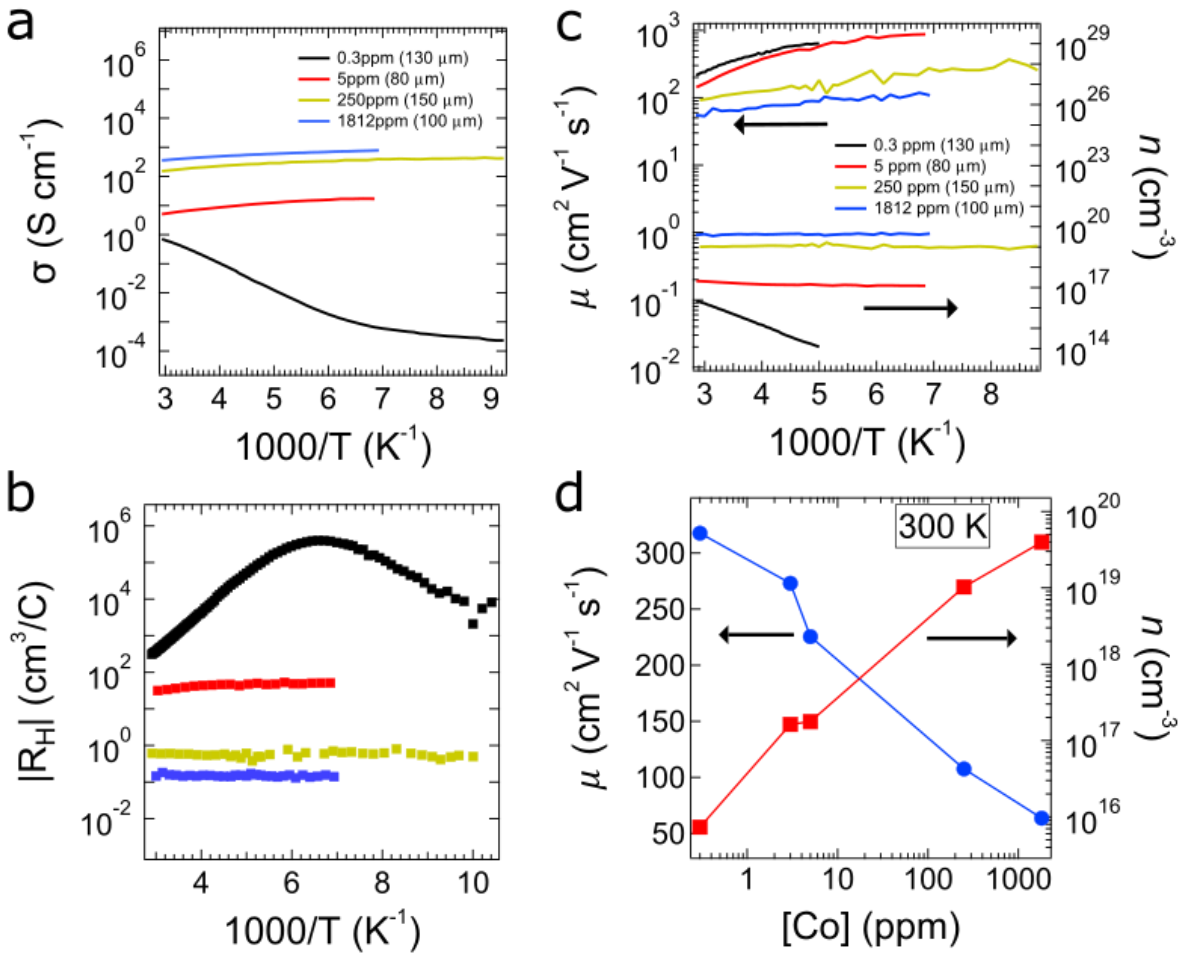

Figure 4.2. Electrical properties of $Co_xFe_{1-x}S_2$ crystals. (a) Conductivity and (b) absolute Hall coefficient versus inverse temperature for samples with various Co concentrations, from .3 ppm (for an undoped control crystal) to 1812 ppm. (c) Bulk electron density (n) and mobility (μ) in the unambiguously unipolar (n-type) temperature region. (d) Room-temperature n and μ as a function of [Co].

In a semiconductor the number of ionized donors N_D^+ can be determined from

$$N_D^+ = \frac{N_D}{1+2\ exp[\frac{E_F - E_D}{kT}]}. \quad (4.1)$$

Where N_D is the donor concentration and E_F is the Fermi the energy of the system. The number of free carriers n in the system can also be calculated using

$$n = N_C \frac{2}{\sqrt{\pi}} F_{\frac{1}{2}}(\frac{E_F - E_C}{kT}), \quad (4.2)$$

where N_C is the effective density of states in the conduction band, under the parabolic band approximation, and $F_{1/2}$ is the Fermi integral given by

$$F_{1/2}(\eta_f) = \int_0^\infty \frac{\eta^{1/2}\, d\eta}{1+exp(\eta - \eta_f)}. \quad (4.3)$$

Equations (6) and (7) can be equated using the charge neutrality condition, $n \cong N_D^+$. From this a self-consistent Fermi energy can be determined from a given donor level (E_D-E_C) and N_D then can be used to calculate n or N_D^+. In non-degenerate semiconductors the condition that $(E_F - E_C) > 3kT$, allows one to use Boltzmann statistics to greatly simplify Eq.4.2 to obtain an analytic solution. For the case of degenerate semiconductors, this condition is not met and Eq.4.2 must be solved numerically. Taking this degeneracy into account we find that as N_D is increased n also increases (and hence N_D^+), until the Fermi level rises to the point where the

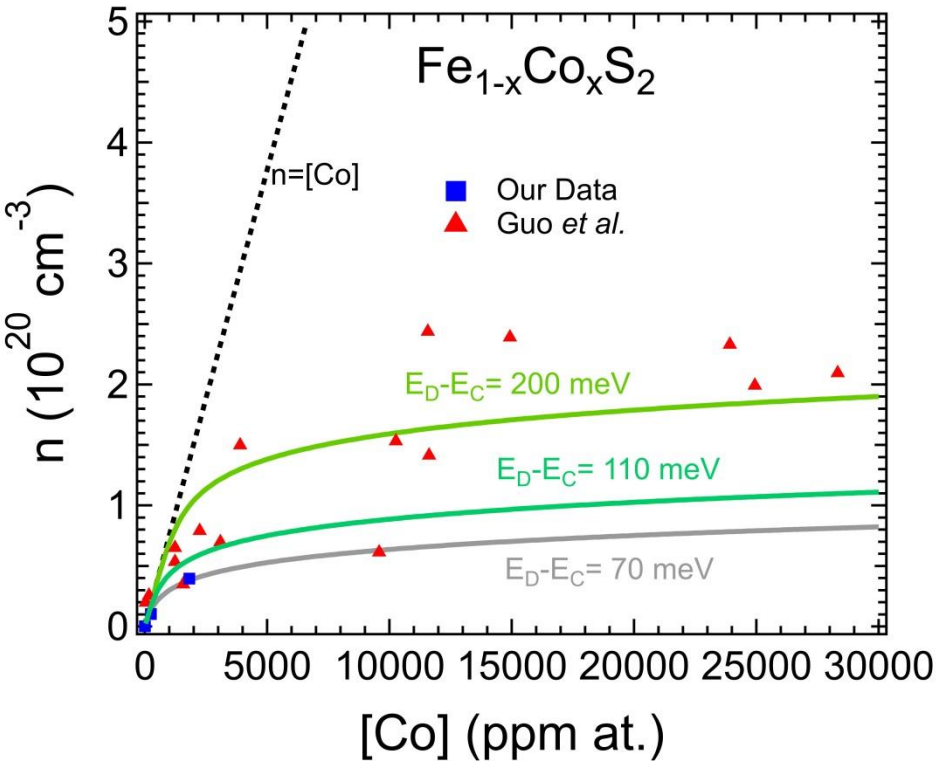

Figure 4.3. Number of charge carriers as a function of Co concentration. Blue squares represent the data shown in Fig. 4.2d, while the red triangles are adapted from [40]. The dashed line shows n if every Co atom contributes one electron. The solid lines are fits to the joint data where $E_c - E_d$ is allowed to float. The upper line is a fit of the entire joint data set resulting in a defect state ~200 meV above E_C, while the middle line is a fit to [Co] < 4000 ppm giving us E_D-E_C = 120 meV. The bottom solid line is a fit to only our data resulting in $E_D - E_C$ = 70 meV.

probability of occupying the defect state is non-negligible, making $\frac{N_D^+}{N_D} < 1$. Fits to our data place the defect state ~70 meV above the conduction band minimum. However, since we look only at dilute doping cases in our study, this effect is not prominent in our data set with only our largest doping concentration showing a drastic decrease in ionization efficiency. Guo *et al.* showed that while n increased with increasing [Co] for concentrations below 8000ppm, n was relatively constant for [Co] > 8000ppm [40]. This behavior is well captured when taking into account the effects of degeneracy on ionization efficiency. Least square fits of our joint data sets (using only Guo *et al.*'s low [Co] (< 4000 ppm) data) place the defect state ~110meV above

E_C (see Fig. 4.3). However, it must be noted that the validity of [Co] in the low [Co] range of Guo et.al.'s data is called into question since the concentration was calculated from the magnetization saturation [41]. In the low [Co] range, as we can see from our electrical data, a large majority of the Co donates an electron to the conduction band and therefore is in the low-spin Co^{3+} resulting in no magnetic moment. This implies that the concentration of [Co] in [40] is overestimated in the low [Co] regime. Correcting for this would push the E_D from fits closer to E_C. While this model is oversimplified, in that it assumes the donor density of states is a delta function at E_D and neglects changes to the shape of the conduction band with increased doping, it gives us a qualitative means of understanding the reduction in donor efficiency and helps give us an approximate location of our defect state within our conduction band (70 – 110 meV above E_C).

4.2 Nickel Doped ($Ni_xFe_{1-x}S_2$)

Nickel-containing pyrite crystals were made using 99.996% nickel powder dissolved in hydrazine as the nickel source and incorporated into the synthesis in the same manner that the Co precursor was added to the Co-doped samples. Using this method, samples with [Ni] ranging from 8 to 17,942 ppm were fabricated and the structural and electronic properties were thoroughly characterized to give us a clear understanding of the effects of Ni doping.

4.2.1 Elemental Characterization

We use ICP-MS to quantify the concentration of Ni in our doped samples as well as the 60 other elements measured by ICP-MS. Results indicate a Ni content of 8 to 17,942 ppm our Ni-doped crystals, increasing roughly in proportion to the amount of nickel spiked in the flux. Three crystals were sectioned into slab parallel to the top facet and some of those slabs were fractured in half before each was dissolved in acid and measure by ICP-MS to check for Ni inhomogeneity in our samples. We found that two of the crystals were evenly doped throughout the crystal while one sample have a two-fold lower [Ni] in its topmost section (Table 4.4). The reason for such a drastic gradient in that sample is not yet understood, but the consistency in the other measurements give us reason to believe that a majority of the samples are uniformly doped and we will treat them as such for the duration of this section. However, we attempted to measure [Ni] on the exact sample to in the other characterization techniques whenever possible. Full elemental analysis of a 558 ppm Ni sample shows us that the addition of Ni into our sample didn't unintentionally add other impurities to our crystals (Table 4.5).

Sample	**Ni:Fe Added**	**Section***	**[Ni] (ppm at.)**	Average [**Ni**] (**atoms/cm^{-3}**)	***x***
1	.00047	1	29	1.9×10^{18}	8×10^{-5}
		2a	28		
		2b	24		
2	.00095	1	323	3.7×10^{19}	0.0016
		2a	623		
		2b	535		
		3	588		
3	.0019	1	1187	7.8×10^{19}	0.0033
		2	989		

Table 4.4. [Ni] uniformity in $Ni_xFe_{1-x}S_2$ crystals.* Section 1 refers to the top of the crystal and section 3 to the bottom of the crystal (a and b refer to pieces of the crystal in the same z-section, measured to check for homogeneity in the xy plane).

558 ppm Ni Sample			
S:Fe = 1.8144[b]			
element	**ppm at**	**element**	**ppm at**
Na	19.9891	Te[a]	0.0017
Mg	2.1924	Cs	0.0014
Sc	0.0696	Ba	<0.05
Ti	0.20799	La	0.0003
V	0.0212	Ce	0.0006
Cr	2.8758	Pr[a]	<0.001
Mn	0.3184	Nd	<0.003
Co	0.1147	Sm	0.0001
Ni	558.6	Eu	<0.0001
Cu	<3.28	Gd	<0.0004
Zn	4.6496	Tb	0.0010
Ga	0.0033	Dy	<0.0001
Ge	0.0048	Ho	<0.0002
As	<0.11	Er	<0.0001
Se	<0.01	Tm	<0.0001
Rb	0.0205	Yb	<0.0002
Sr	0.0151	Lu	0.0014
Y[a]	0.0005	Hf[a]	<0.0001
Zr[a]	<0.04	Ta[a]	<0.0001
Nb[a]	0.0001	W[a]	0.0003
Mo[a]	<0.017	Re[a]	0.0026
Ru[a]	0.1203	Os[a]	0.00044
Rh[a]	0.0104	Ir[a]	0.00026
Pd[a]	0.0051	Pt[a]	0.0030
Ag	0.0005	Au[a]	0.0001
Cd	0.0007	Hg[a]	0.0818
In	0.0041	Tl	0.0001
Sn[a]	0.0002	Pb	<0.04
Sb[a]	0.0002	Bi	0.0029
		U	0.0065

Table 4.5: ICP-MS results of a typical Ni-doped ([Ni] = 558 ppm) crystal reported in atomic ppm. [a] Elemental concentration determined by semi-quantitative methods. [b] Due to sulfur loss during sample preparation, the measured S:Fe deviates from the expected 2:1.

4.2.2 Structural Characterization

As with the Co-doped crystals, the Ni-containing crystals had similar size, shape, faceting, and overall quality as our undoped crystals. Synchrotron XRD patterns suggest that crystals with relatively low Ni content (<1500 ppm, $x < 0.0045$) are phase pure and homogeneous. While we see several peaks in the 517 ppm XRD pattern (red asterisks in Fig. 4.4a) that don't belong to pyrite, they index to cristobalite (SiO_2) and are likely a surface contaminate from sample preparation rather than a phase impurity in the bulk of our crystal. Higher Ni levels result in increasingly broadened, asymmetric line shapes consistent with a highly inhomogeneous distribution of Ni that induces a range of lattice constants in individual crystals (Figure 4.4a). Since NiS_2 (vaesite, a = 5.670 Å) and FeS_2 (a = 5.417 Å) are reported to form partial $Ni_xFe_{1-x}S_2$ solid solutions with a maximum NiS_2 solubility in pyrite of only $x = 0.073$ at 729°C and probably much lower equilibrium solubility close to room temperature (likely <1000 ppm) [47,48], high Ni loadings are anticipated to cause compositional heterogeneity, metastable solid solutions, and phase separation. In addition to asymmetric peak broadening toward larger d-spacing, we sometimes observed minor phase impurities in crystals with higher Ni content (Fig. 4.4). To avoid complications originating from non-uniform composition, we focus most of our attention on crystals with [Ni] < 1500 ppm.

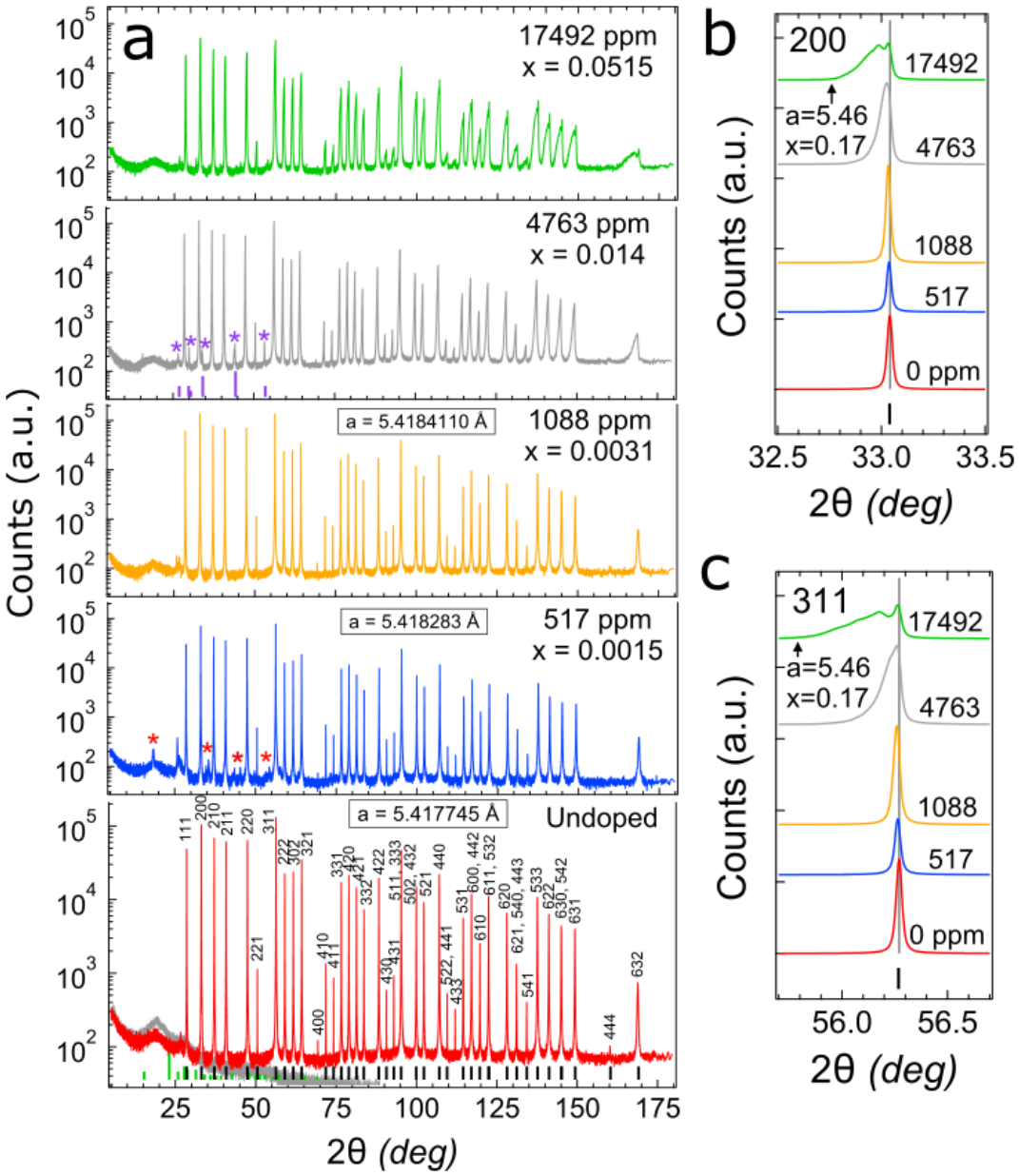

Figure 4.4. Synchrotron powder XRD patterns of $Ni_xFe_{1-x}S_2$ crystals. (a) Data on a log scale for $Ni_xFe_{1-x}S_2$ samples with x = 0.0, 0.0016, 0.0033, 0.014, and 0.0525. Purple asterisks denote an impurity phase in the x = 0.014 sample. The impurity peaks are consistent with "$Fe_8Ni_8S_{16}$" (PDF 00-022-0627, purple bars) or $FeNiS_2$ (PDF 01-071-4458). Red asterisks mark peaks that belong to SiO_2 (PDF 00-003-0257), likely a contaminate from sample prep. Overlaid on the undoped data are a background pattern of an empty capillary tube (gray) as well as reference patterns for pyrite (black bars) and orthorhombic sulfur (green bars). (b,c) Magnified views of the 200 and 311 reflections, showing significant broadening and distortion of the peaks toward smaller 2Θ (larger d-spacing) for x > 0.0033. The broad, asymmetric reflections indicate that the two samples with the highest [Ni] are not single-phase $Ni_xFe_{1-x}S_2$ solid solutions.

4.2.3 Hall Effect Studies

Conductivity and Hall data for Ni-containing crystals show that Ni impurities have little impact on the electrical properties of pyrite (Figure 4.8). Near room temperature, where the undoped control crystals and all of the Ni-containing crystals are unambiguously *n*-type due to ionization of bulk donors, we find that $\sigma(T)$ is independent of [Ni] for [Ni] < 1000 ppm and actually *decreases* for higher [Ni] because of a reduced carrier mobility. The electron concentration shows some spread (10^{15}-10^{16} cm^{-3} at 300 K) but is clearly uncorrelated with [Ni]. We also note a large increase in the activation energy of $\sigma(T)$ for samples with [Ni] > 1000 ppm. From section 4.2.2, we know that samples with this high of a Ni concentration show phase impurities and large crystal strain. It appears, for these samples conduction is dominated by these impurities which greatly alter electronic behavior. However, because of the poor properties of these crystals they are of limited interest to us and were not explored further. From these data, we conclude that Ni_{Fe} is either a very deep donor (at least 400 meV below the conduction band edge) or completely compensated by accompanying acceptor defects. Either way, Ni is not a significant dopant in pyrite. Our assessment agrees with the EPR results of Chandler and Bené on CVT-grown $Ni_xFe_{1-x}S_2$ crystals made using Cl_2 transport (with x estimated from nuclear activation analysis to be $0.0004 \leq x \leq 0.03$) [32] as well as the Hall measurements of Lehner and co-workers on CVT crystals made with $FeBr_3$ as the transport agent ($0.005 \leq x \leq 0.01$ by secondary ion mass spectrometry) [25,36]. However, our results disagree with the

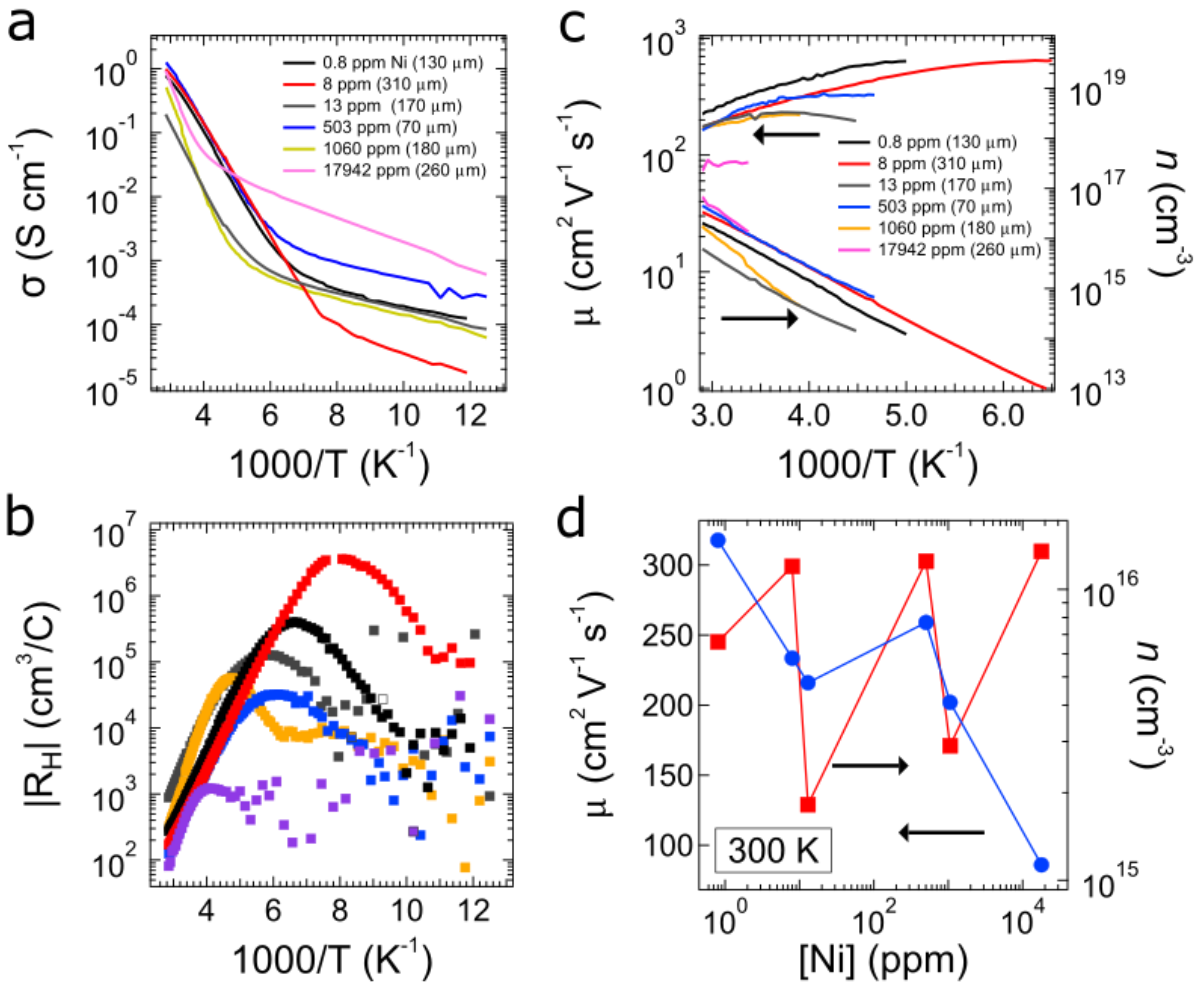

Figure 4.8. Electrical properties of $Ni_xFe_{1-x}S_2$ crystals. (a) Conductivity and (b) absolute Hall coefficient versus inverse temperature for samples with various nickel concentrations, from 0.8 ppm (for an undoped control crystal) to 17,942 ppm. (c) Bulk electron density (n) and mobility (μ) in the unambiguously unipolar (n-type) temperature region. (d) Room-temperature n and μ as a function of [Ni].

findings of Ho *et al.*, who reported that $\sigma(T)$ increases with [Ni] for $Ni_xFe_{1-x}S_2$ alloys (with x = 0.01, 0.02, 0.04, and 0.1, although no elemental analysis was reported) made by CVT using ICl_3 as the transport agent [33,34]. The latter results can be understood if ICl_3 somehow reduces the concentration of compensating defects or results in the formation of Ni defect complexes (possibly with I^- and/or Cl^-) that act as reasonably shallow donors in pyrite.

4.3 Chromium Doped ($Cr_xFe_{1-x}S_2$)

Cr was added to the crystal synthesis in the form of 99.99% $Cr(NO_3)_3 \bullet 9H_2O$ dissolved in methanol before being added to the growth crucible completeing the flux growth protocal in the same manner as the Co and Ni samples were. Samples were made with Cr concentrations ranging from 39 to 5187 ppm. The electric properties of these crystals will be discussed in the following sections.

4.3.2 Elemental Characterization

Using ICP-MS and the same technique as we did with the Co and Ni doped crystals, we looked at the homogeneity of our Cr incorporation in one of our crystals. We find that the uniformity of Cr in the sample is excellent in all but one of the pieces measured, which had a ~30% lower concentration of Cr. The reason for this difference is not quite known, however the excellent agreement across the rest of the sample leads one to think it may have been an artifact of

Sample	Cr:Fe Added	Section*	[Cr] (ppm at.)	Average [Cr] (atoms/cm^{-3})	x
1	0.0022	1a	411	3.1×10^{19}	0.0012
		1b	465		
		2a	294		
		2b	438		
		3a	436		
		3c	424		

Table 4.8. [Cr] uniformity in $Cr_xFe_{1-x}S_2$ crystals. * Section 1 refers to the top of the crystal and section 3 to the bottom of the crystal (a and b refer to pieces of the crystal in the same z-section, measured to check for homogeneity in the xy plane).

cause by sample preparation. Attempts were still made to measure the exact crystal used in the other measurement techniques whenever possible. As with Co and Ni, we found that Cr could be incorporated into the crystals without substantially increasing the concentration of the other elements measured by ICP-MS (Table 4.9). We do see a slightly higher Zn and Mn concentration than is typical of undoped crystals, but is not outside of the values seen.

4.3.1 Structural Characterization

Crystals synthesised with our Cr precuror show similar size, shape, faceting, and overall quality as our undoped crystals. Sycrotron XRD patterns taken of crystals with up to 5187 ppm suggest that all samples are single-phase, homogeneous $Cr_xFe_{1-x}S_2$ solid solutions with lattice constants that increase monotonically with x over the range studied ($0 \leq x \leq 0.0149$, Fig. 4.6).

33 ppm Cr Sample			
S:Fe = 1.95022562			
element	**ppm at**	**element**	**ppm at**
Na	172.4187	Te[a]	0.0204
Mg	4.3873	Cs	<0.009
Sc	0.0873	Ba	<0.072
Ti	0.0417	La	0.0001
V	0.0326	Ce	0.0002
Cr	33.2700	Pr	0.0002
Mn	0.2949	Nd	0.0008
Co	0.1009	Sm	0.0001
Ni	0.5440	Eu	<0.0001
Cu	0.5353	Gd	0.0001
Zn	7.0815	Tb	0.0026
Ga	0.0105	Dy	0.0001
Ge	0.0322	Ho	0.0005
As	<0.0016	Er	<0.0003
Se	<0.004	Tm	<0.0001
Rb	<0.0296	Yb	<0.0003
Sr	0.0146	Lu	0.0035
Y[a]	0.0001	Hf[a]	0.0008
Zr[a]	0.0229	Ta[a]	0.0001
Nb[a]	0.0021	W[a]	0.0014
Mo[a]	0.0051	Re[a]	0.0005
Ru[a]	0.0698	Os[a]	0.0001
Rh[a]	0.0116	Ir[a]	0.0001
Pd[a]	0.0074	Pt[a]	0.0008
Ag	0.1051	Au[a]	0.0004
Cd	<0.0007	Hg[a]	0.1626
In	0.0108	Tl	<0.0003
Sn[a]	0.0075	Pb	0.0035
Sb[a]	0.0075	Bi	0.0079
		U	<0.0006

Table 4.9: ICP-MS results of a typical Cr-doped ([Cr] = 33 ppm) crystal reported in atomic ppm. [a] Elemental concentration determined by semi-quantitative methods.

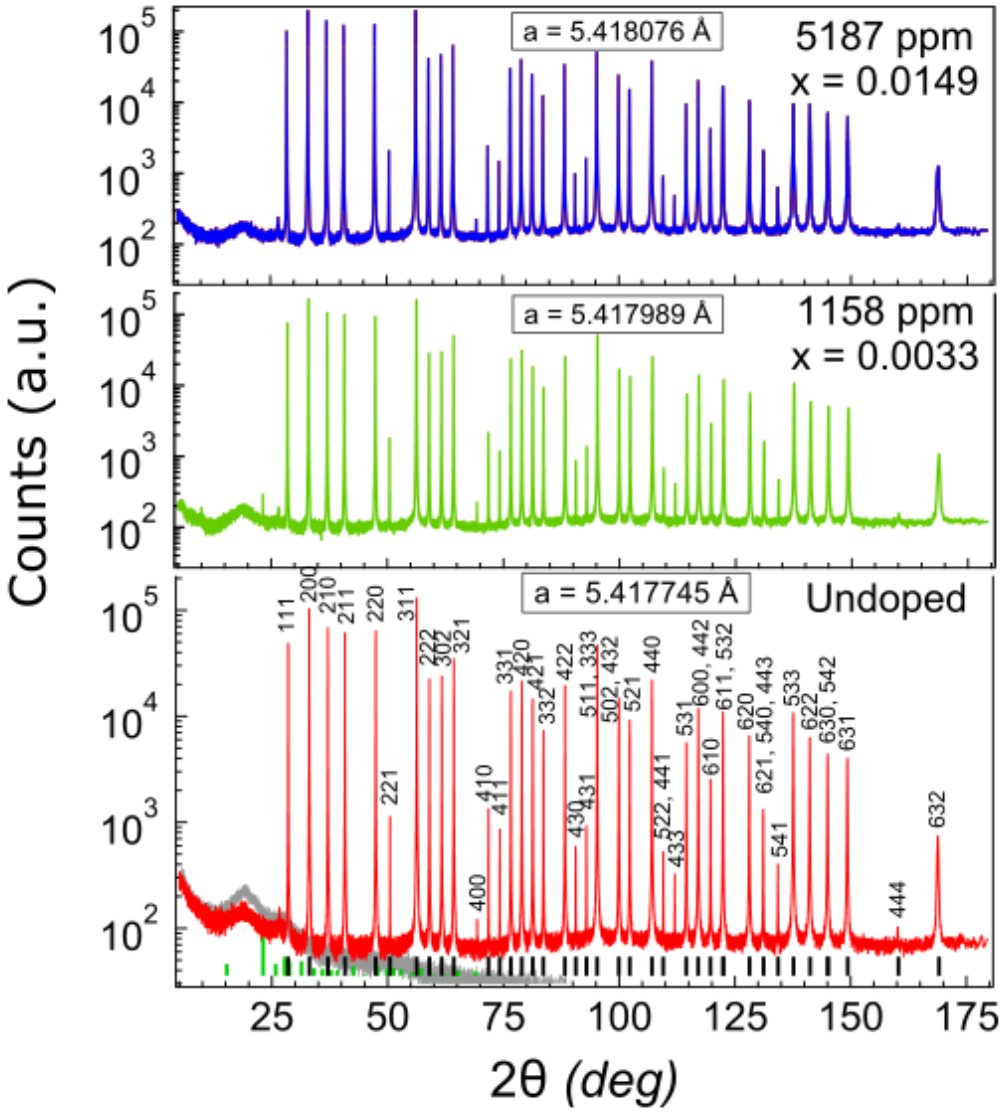

Figure 4.6. Synchrotron XRD pattern of a powdered undoped and powdered $Cr_xFe_{1-x}S_2$ crystals with x = 0.0033 and 0.0149, presented on a log scale. All 39 reflections index to pyrite and no other phases are detected. Lattice parameters were calculated by Rietveld refinement with PDXL2 software at room temperature. The background pattern is for an empty capillary tube. Overlaid on the undoped data are a background pattern of an empty capillary tube (gray) as well as reference patterns for pyrite (black bars) and orthorhombic sulfur (green bars).

4.3.3 Hall Effect Studies

Chromium addition has a small but noticeable impact on the electrical properties of the pyrite crystals. Figure 4.7 shows that $\sigma(T)$ and $|R_H|(T)$ of the $Cr_xFe_{1-x}S_2$ and undoped crystals are qualitatively similar from 80-350 K. As with the $Ni_xFe_{1-x}S_2$ samples, all of the $Cr_xFe_{1-x}S_2$ crystals are unipolar *n*-type at higher temperatures. In this temperature regime, we find that $\sigma(T)$ rises and then levels off with increasing [Cr], reflecting a competition between increasing electron density and decreasing electron mobility (Fig. 4.7c-d). The room-temperature electron density increased tenfold and the mobility decreased by a factor of two across the range of [Cr] we studied (from 3×10^{17} to 4×10^{20} atoms cm^{-3}). The chromium doping efficiency ($\Delta n/\Delta$[Cr]) is low and decreases from ~0.01 at low [Cr] to $\sim10^{-4}$ at high [Cr], suggesting that Cr_{Fe} is a deep donor that becomes increasingly compensated at higher doping density. We conclude that Cr acts as a donor in pyrite, but a very poor one.

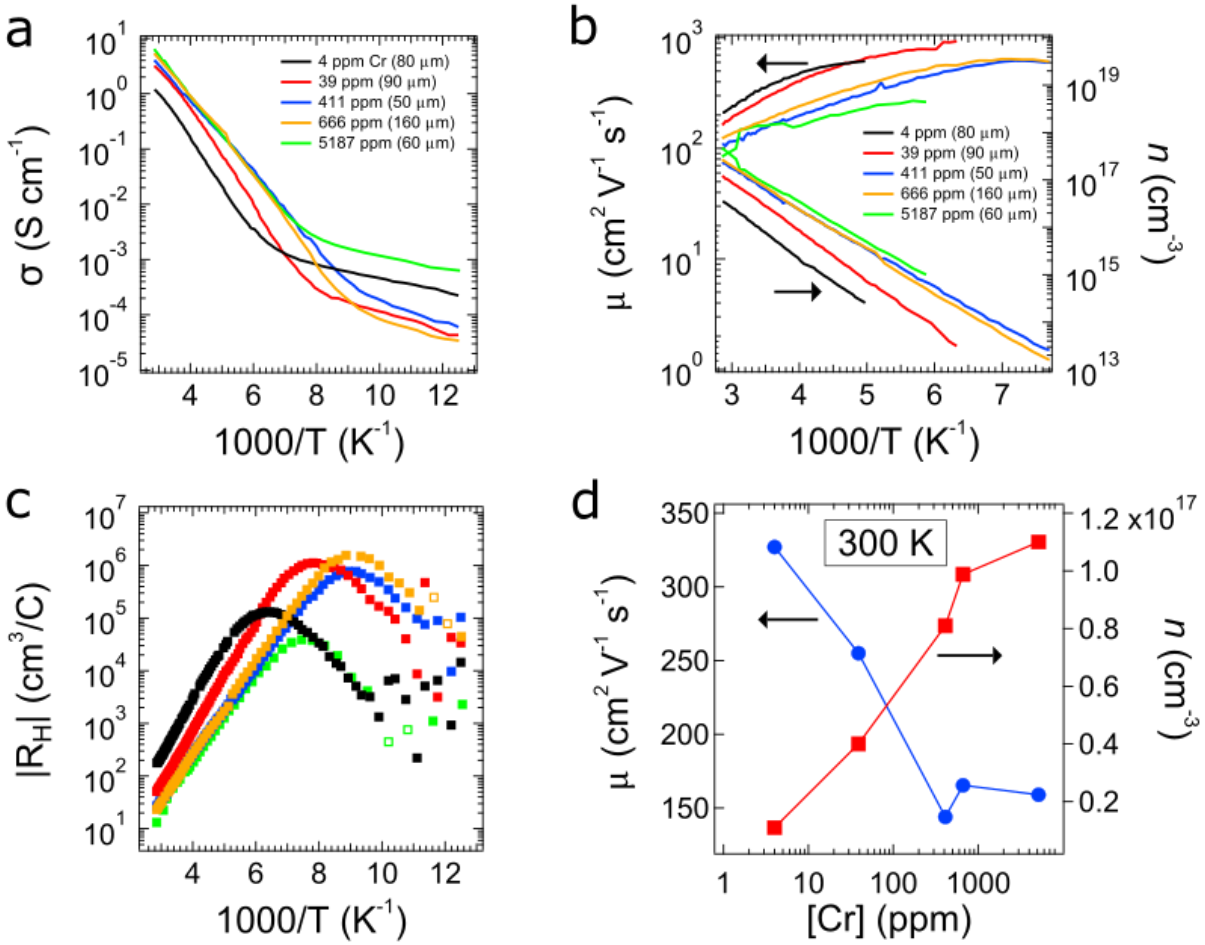

Figure 4.7. Electrical properties of $Cr_xFe_{1-x}S_2$ crystals. (a) Conductivity and (c) absolute Hall coefficient versus inverse temperature for samples with various chromium concentrations, from 4 ppm (for an undoped control crystal) to 5187 ppm. (b) Bulk electron density (n) and mobility (μ) in the unambiguously unipolar (n-type) temperature region. (d) Room-temperature n and μ as a function of [Cr].

4.4 Conclusions

We have studied the impact of Co, Ni, and Cr impurities on the electrical, optical, and magnetic properties of high-purity iron pyrite single crystals grown in sodium polysulfide flux. Without added Co, Ni, or Cr, the pyrite crystals are chemically pure (>99.998% on a metals basis) but still *n*-type near room temperature due to unintentional doping by $\sim 10^{19}$ cm^{-3} native deep donors, probably sulfur vacancies. These crystals have relatively low room-temperature carrier density (2×10^{15} cm^{-3}) and high mobility (300 cm^2 V^{-1} s^{-1}).

Cobalt is a well-behaved donor in pyrite with a defect state located above the conduction band minimum. We find a high doping efficiency at low [Co] (< 500 ppm). At these concentrations, cobalt should be nonmagnetic Co^{3+} (t_{2g}^6 electron configuration), consistent with full ionization. Samples with [Co] > 5 ppm show $n > 10^{17}$ cm^{-3} at 300 K and metallic $\sigma(T)$ plots. The bulk electrons from Co_{Fe} do not freeze out, so the transition from bulk to surface conduction normally seen in pyrite at lower temperatures does not occur in $Co_xFe_{1-x}S_2$ samples. From analysis of the ionization efficiency we derive a Co defect state that lies 70 - 110 meV above the conduction band edge. Cobalt is currently the best *n*-type dopant for pyrite because it offers high solubility and doping efficiency with minimal compensation, mobility degradation, and magnetism (for [Co] < 500 ppm), enabling controlled doping to achieve a wide range of electron

concentrations (10^{15}-10^{20} cm^{-3}). For [Co] > 1000 ppm, the doping efficiency steadily decreases, as expected from previous work on $Co_xFe_{1-x}S_2$ alloys (x > 0.005).

Single-phase, homogeneous $Ni_xFe_{1-x}S_2$ samples could be made only for [Ni] < 1500 ppm. Higher Ni content results in a phase mixture of solid solutions. Nickel at all concentrations does not significantly alter the carrier concentration of pyrite, therefore its defect state must lie deep within the band gap likely > 400 meV below the conduction band. Except for causing degradation in electron mobility, Ni by itself seems to be a rather inert impurity in iron pyrite. Still future devices would benefit from reducing the Ni contamination in order to boost mobilities and increase device performance.

Chromium acts as a deep donor with a doping efficiency that drops with increasing [Cr], making it a poor dopant in pyrite. Since we see some contribution to the carrier concentration by Cr we know its defect state lies above that of Ni, but is still several hundred meV below the band edge. Cr also degrades the electron mobility by about a factor of two. Given the position of the defect state within the band gap, we conclude Cr would be detrimental to pyrite device performance, acting both as a scattering center for transport as well as a possible recombination center and its unintentional incorporation should be minimized.

This study shows that progress in understanding and controlling the doping of iron pyrite can be achieved through combined electrical, optical, and magnetic measurements of ultrapure single crystals spiked with individual impurity elements. Using this approach, we have found that cobalt is an excellent *n*-type dopant, while nickel and chromium act as deep donors that hardly affect the carrier concentration. This work establishes the electronic behavior of these

three transition metal impurities, but many important open questions remain for further study. Identifying and then controlling the concentration of the native deep donor(s) responsible for the unintentional *n*-type doping of pyrite crystals remains a critical challenge in the controlled doping of this material for optoelectronic applications. Discovering a well-behaved shallow acceptor and translating the single crystal results to thin films are also useful directions.

References

[1] BP, *Statistical Review of World Energy* (2019).
[2] U.S. Energy Information Administration, *International Energy Outlook 2019* (2019).
[3] DOE, (n.d.).
[4] NREL, (2019).
[5] C. Wadia, A. P. Alivisatos, and D. M. Kammen, Environ. Sci. Technol. **43**, 2072 (2009).
[6] S. Rühle, Sol. Energy (2016).
[7] A. Ennaoui, S. Fiechter, C. Pettenkofer, N. Alonsovante, K. Buker, M. Bronold, C. Hopfner, and H. Tributsch, Sol. Energy Mater. Sol. Cells **29**, 289 (1993).
[8] A. Ennaoui, S. Fiechter, W. Jaegermann, and H. Tributsch, J. Electrochem. Sci. Technol. **133**, 97 (1986).
[9] J. Hu, Y. Zhang, M. Law, and R. Wu, J. Am. Chem. Soc. **134**, 13216 (2012).
[10] R. Schieck, A. Hartmann, S. Fiechter, R. Könenkamo, and H. Wetzel, J. Mater. Res. **5**, 1567 (1990).
[11] G. Smestad, A. Ennaoui, S. Fiechter, H. Tributsch, W. K. Hofmann, M. Birkholz, and W. Kautek, Sol. Energy Mater. **20**, 149 (1990).
[12] A. Ennaoui and H. Tributsch, Sol. Energy Mater. **14**, 461 (1986).
[13] P. P. Altermatt, T. Kiesewetter, K. Ellmer, and H. Tributsch, Sol. Energy Mater. Sol. Cells **71**, 181 (2002).
[14] M. Bronold, C. Pettenkofer, and W. Jaegermann, J. Appl. Phys. **76**, 5800 (1994).
[15] R. Murphy and D. R. Strongin, Surf. Sci. Rep. **64**, 1 (2009).
[16] M. Limpinsel, N. Farhi, N. Berry, J. Lindemuth, C. L. Perkins, Q. Lin, and M. Law, Energy Environ. Sci. **7**, 1974 (2014).
[17] S. Seefeld, M. Limpinsel, Y. Liu, N. Farhi, A. Weber, Y. Zhang, N. Berry, Y. J. Kwon, C. L. Perkins, J. C. Hemminger, R. Wu, and M. Law, J. Am. Chem. Soc. **135**, 4412 (2013).
[18] J. Walter, X. Zhang, B. Voigt, R. Hool, M. Manno, F. Mork, E. S. Aydil, and C. Leighton, Phys. Rev. Mater. **1**, 065403 (2017).
[19] M. Cabán-Acevedo, N. S. Kaiser, C. R. English, D. Liang, B. J. Thompson, H. E. Chen, K. J. Czech, J. C. Wright, R. J. Hamers, and S. Jin, J. Am. Chem. Soc. **136**, 17163 (2014).
[20] Y. N. Zhang, J. Hu, M. Law, and R. Q. Wu, Phys. Rev. B - Condens. Matter Mater. Phys. **85**, 1 (2012).
[21] F. W. Herbert, A. Krishnamoorthy, K. J. Van Vliet, and B. Yildiz, Surf. Sci. **618**, 53 (2013).
[22] K. Büker, N. Alonso-Vante, and H. Tributsch, J. Appl. Phys. **72**, 5721 (1992).
[23] M. Bronold, K. Buker, S. Kubala, C. Pettenkofer, and H. Tributsch, **231**, (1993).
[24] M. Birkholz, S. Fiechter, A. Hartmann, and H. Tributsch, Phys. Rev. B **43**, 11926 (1991).

[25] S. W. Lehner, N. Newman, M. Van Schilfgaarde, S. Bandyopadhyay, K. Savage, and P. R. Buseck, J. Appl. Phys. **111**, 0 (2012).
[26] B. Voigt, W. Moore, M. Manno, J. Walter, J. D. Jeremiason, E. S. Aydil, and C. Leighton, ACS Appl. Mater. Interfaces **11**, 15552 (2019).
[27] J. Sangster and A. D. Pelton, J. Phase Equilibria **18**, 89 (1997).
[28] M. Levy and M. P. Sarachik, Rev. Sci. Instrum. **60**, 1342 (1989).
[29] R. L. Petritz, Phys. Rev. **110**, 1254 (1958).
[30] S. M. Sze and K. K. Ng, *Physics of Semiconductor Devices* (Wiley-Interscience, 2007).
[31] D. Liang, M. Cabán-Acevedo, N. S. Kaiser, and S. Jin, Nano Lett. **14**, 6754 (2014).
[32] R. Chandler and R. Bené, Phys. Rev. B **8**, 4979 (1973).
[33] C. H. Ho, C. E. Huang, and C. C. Wu, J. Cryst. Growth **270**, 535 (2004).
[34] C.-H. Ho, M.-H. Hsieh, and Y.-S. Huang, J. Electrochem. Soc. **155**, H254 (2008).
[35] K. S. Savage, D. Stefan, and S. W. Lehner, Appl. Geochemistry **23**, 103 (2008).
[36] S. W. Lehner, K. S. Savage, and J. C. Ayers, J. Cryst. Growth **286**, 306 (2006).
[37] Y. Tomm, R. Schieck, K. Ellmer, and S. Fiechter, J. Cryst. Growth **146**, 271 (1995).
[38] S. R. Butler and R. J. Bouchard, J. Cryst. Growth **10**, 163 (1971).
[39] B. Thomas, K. Ellmer, W. Bohne, J. Röhrich, M. Kunst, and H. Tributsch, Solid State Commun. **111**, 235 (1999).
[40] S. Guo, D. P. Young, R. T. MacAluso, D. A. Browne, N. L. Henderson, J. Y. Chan, L. L. Henry, and J. F. Ditusa, Phys. Rev. B - Condens. Matter Mater. Phys. **81**, 1 (2010).
[41] S. Guo, D. P. Young, R. T. MacAluso, D. A. Browne, N. L. Henderson, J. Y. Chan, L. L. Henry, and J. F. Ditusa, Phys. Rev. B - Condens. Matter Mater. Phys. **81**, 1 (2010).
[42] S. Ogawa, J. Phys. Soc. Japan **41**, 462 (1976).
[43] H. S. Jarrett, W. H. Cloud, R. J. Bouchard, S. R. Butler, C. G. Frederick, and J. L. Gillson, Phys. Rev. Lett. **21**, 617 (1968).
[44] K. Sato, Prog. Cryst. Growth Charact. **11**, 109 (1985).
[45] J. F. Gibbons and R. E. Tremain, Appl. Phys. Lett. **26**, 199 (1975).
[46] P. R. C. Stevens and A. W. Tinsley, J. Phys. C Solid State Phys. J. Phys. C Solid State Phys **4**, L150 (1971).
[47] L. A. Clark and G. Kullard, Econ. Geol. **58**, 853 (1963).
[48] P. Waldner and A. D. Pelton, Metall. Mater. Trans. B **35**, 897 (2004).